

Generation of Low-Latitude Seamount-Trapped Waves: A Case Study of the Seychelles Plateau

Key Points:

- Model output suggests Yanai waves generate trapped waves around the Seychelles Plateau
- Yanai wave energy flux is surface-intensified along the western and south-western plateau edges
- Trapped waves flux energy throughout the water column and around the plateau circumference

Isabella B. Arzeno-Soltero¹ , Sarah N. Giddings² , Geno Pawlak^{2,3} , Julie L. McClean² , He Wang⁴ , Luc Rainville⁵ , and Craig M. Lee⁵

¹Civil and Environmental Engineering, University of California, Irvine, CA, USA, ²Scripps Institution of Oceanography, University of California, San Diego, CA, USA, ³Department of Mechanical and Aerospace Engineering, University of California, San Diego (UCSD), San Diego, CA, USA, ⁴University Corporation for Atmospheric Research/NOAA Geophysical Fluid Dynamics Laboratory, Boulder, CO, USA, ⁵Applied Physics Laboratory, University of Washington, Seattle, WA, USA

Correspondence to:

I. B. Arzeno-Soltero,
iarzeno@alumni.stanford.edu

Citation:

Arzeno-Soltero, I. B., Giddings, S. N., Pawlak, G., McClean, J. L., Wang, H., Rainville, L., & Lee, C. M. (2021). Generation of low-latitude seamount-trapped waves: A case study of the Seychelles Plateau. *Journal of Geophysical Research: Oceans*, 126, e2021JC017234. <https://doi.org/10.1029/2021JC017234>

Received 29 JAN 2021

Accepted 1 JUL 2021

Abstract Baroclinic seamount-trapped waves are thought to influence their surrounding ecosystem; however, trapped waves are not well-studied in near-equatorial settings, where stratification is strong and Burger numbers $\left(S = \frac{N^2 H^2}{f^2 L_H^2} \right)$ are large. Motivated by observations, we use daily output (2005–2009) from the global Parallel Ocean Program Model (POP) to examine topographically trapped baroclinic waves around the Seychelles Plateau ($S > 400$) in the tropical Indian Ocean. These trapped waves are associated with velocity and temperature oscillations at periods of 15–16 days, similar to the dominant period of some equatorial Yanai waves. Energy flux maps using POP output suggest that quasi-biweekly equatorial Yanai waves excite trapped waves on the western and south-western flanks of the Seychelles Plateau, near the surface. The anticyclonic energy flux associated with the trapped wave extends vertically throughout the water column and around most of the plateau circumference, diminishing on the eastern flank of the plateau. This work highlights the role that equatorial planetary waves and trapped waves play in facilitating energy redistribution, dissipation, and mixing in the tropical ocean.

Plain Language Summary Oceanic internal waves (waves in the interior of the ocean) that propagate around seamounts are thought to contribute to ecological productivity, yet there is a lack of research on the dynamics of these processes in the tropics. We refer to these particular internal oscillations as “trapped waves” because they propagate along a topographic slope, rather than radiating away in the ocean as free waves. Motivated by observations, we use five years (2005–2009) of daily output from a global numerical model (POP) to study trapped waves around the Seychelles Plateau in the tropical Indian Ocean. These oscillations cause changes in the velocity and temperature at periods of 15–16 days, resembling the dominant periods of some waves along the equator (Yanai waves). We created maps of energy pathways using POP output; these suggest that Yanai waves excite the plateau-trapped waves near the surface, along the western and south-western flanks of the plateau. The trapped waves propagate energy vertically throughout the water column and around the plateau until they reach the eastern side of the plateau, where the energy decays. This work highlights the role of equatorial waves and trapped waves in redistributing energy, and facilitating turbulence and mixing in the tropical ocean.

1. Introduction

Seamounts have long been lauded as biological hot spots, following evidence that they can retain material including larvae (Chapman & Haidvogel, 1992; Goldner & Chapman, 1997; Mullineau & Mills, 1997) and support elevated biomass (Clark et al., 2010; Dower et al., 1992; Morato et al., 2010; Rowden, Schlacher, et al., 2010). Seamounts have also been recognized as sites with significant mixing and dissipation (Egbert & Ray, 2003; Lueck & Mudge, 1997; Toole et al., 1997). Although the evidence supporting the biological significance of seamounts is still inconclusive (Rowden, Dower, et al., 2010; White et al., 2007), seamounts remain an active area of research due to their ubiquitous nature (Wessel et al., 2010), their potential for bio-physical interactions (Lavelle & Mohn, 2010), and their contributions to mixing and dissipation (Lueck & Mudge, 1997).

An interesting feature of seamounts is their ability to support anticyclonic topographically trapped waves (waves with an evanescent cross shelf wavenumber) that enhance energy from selective subinertial frequencies (Brink, 1990, 1995; Haidvogel et al., 1993). Numerical models show that these trapped waves can be excited by offshore barotropic currents, amplifying energy near the seamount by up to four orders of magnitude relative to that found in the far-field (Brink, 1990; Haidvogel et al., 1993). The resonant frequency of the seamount need not match the exact frequency of the forcing in order to drive a trapped wave (Codiga, 1997; Haidvogel et al., 1993). Although research suggests that any ambient current may generate seamount-trapped waves, many of the existing observational, analytical, and numerical studies focus on trapped waves generated from tidal interactions (e.g., Brink, 1995; Chapman, 1989; Codiga & Eriksen, 1997; Haidvogel et al., 1993; Hunkins, 1986). Since tidal frequencies are only subinertial (trapped, evanescent in the radial direction) at mid- and high- latitudes, research focused on seamount-trapped waves at tidal frequencies leaves a knowledge gap on seamount-trapped waves at low latitudes, though we can rely on some coastal-trapped wave literature (e.g., Brink, 1982) to guide our understanding. Coastal-trapped and seamount-trapped wave dynamics are similar, but there is a coastal barrier in the coastal-trapped wave case while the flow is allowed to cross the summit in the seamount-trapped wave case (compare, e.g., the governing equations in Brink, 1989 and Brink, 1982).

Low latitudes are characterized by having large baroclinic Rossby radii of deformation ($L_R = NH/f$; Chelton et al., 1998). The relationship between the topographic lengthscale (L_H) and L_R influences the features of seamount-trapped waves, analogous to what is seen in coastal-trapped waves (e.g., Huthnance, 1978; Rhines, 1970). This relationship is summarized in the Burger number (S),

$$S = \frac{L_R^2}{L_H^2} = \frac{N^2 H^2}{f^2 L_H^2}, \quad (1)$$

where H is the water depth, N is the buoyancy frequency, f is the Coriolis parameter, and L_H is taken to be a relevant horizontal lengthscale, such as the width of the sloping topography. Trapped waves with large Burger numbers ($S \gg 1$, as can be found in the tropics) are analogous to internal coastal-trapped Kelvin waves (Huthnance, 1978; Rhines, 1970).

Here, we focus on trapped waves near the Seychelles Plateau, a broad semi-elliptical structure in the southwestern equatorial Indian Ocean, extending from approximately 3.5° S to 6.5° S and 53.5° E to 57.5° E (Figure 1a). It is an area of interest given its steep slopes of $O(0.05)$, shallow average depth (60–100 m), large size ($\sim 300 \times \sim 200$ km), and location in a uniquely dynamic tropical ocean with energy at various frequencies that may be resonant with the plateau. The islands on the plateau are small, compared to the plateau size (e.g., the largest island on the plateau, Mahé, is ~ 20 km long by ~ 10 km wide; see Figure 1). Although the Seychelles Plateau is not strictly a seamount, we refer back to seamount-trapped wave literature to describe our work.

The principal atmospheric driver in the Indian Ocean is the seasonal western Indian Ocean monsoon system; during boreal winter (summer), northeasterly (southwesterly) winds are present over India and veer as they cross the Equator, becoming northwesterly (southeasterly) winds over the Seychelles Plateau (Castillo-Trujillo et al., 2020b; Schott & McCreary, 2001; Schott et al., 2009). Equatorial intraseasonal fluctuations in the monsoonal wind stress can generate quasi-biweekly (period around 14 days) Yanai waves in the western basin (50 – 60° E; e.g., Arzeno et al., 2020; Chatterjee et al., 2013; Miyama et al., 2006; Murty et al., 2006; Sengupta et al., 2004). This is noteworthy, since Castillo-Trujillo et al. (2020b) observe that most of the current variability atop the Seychelles Plateau is found at periods of 10–40 days, consistent with the quasi-biweekly Yanai wave period.

Yanai waves (also known as mixed Rossby-gravity waves) are a type of equatorial wave described by their antisymmetric sea level anomalies (ASLA) and identified with the dispersion relation

$$k = \frac{\omega}{c_n} - \frac{\beta}{\omega}, \quad (2)$$

where ω is the frequency, k is the zonal wavenumber, β is the meridional derivative of the Coriolis parameter, and c_n is the n th mode baroclinic Kelvin wave phase speed, following Chatterjee et al. (2013). Quasi-biweekly Yanai waves in the equatorial Indian Ocean have been studied using numerical models (e.g.,

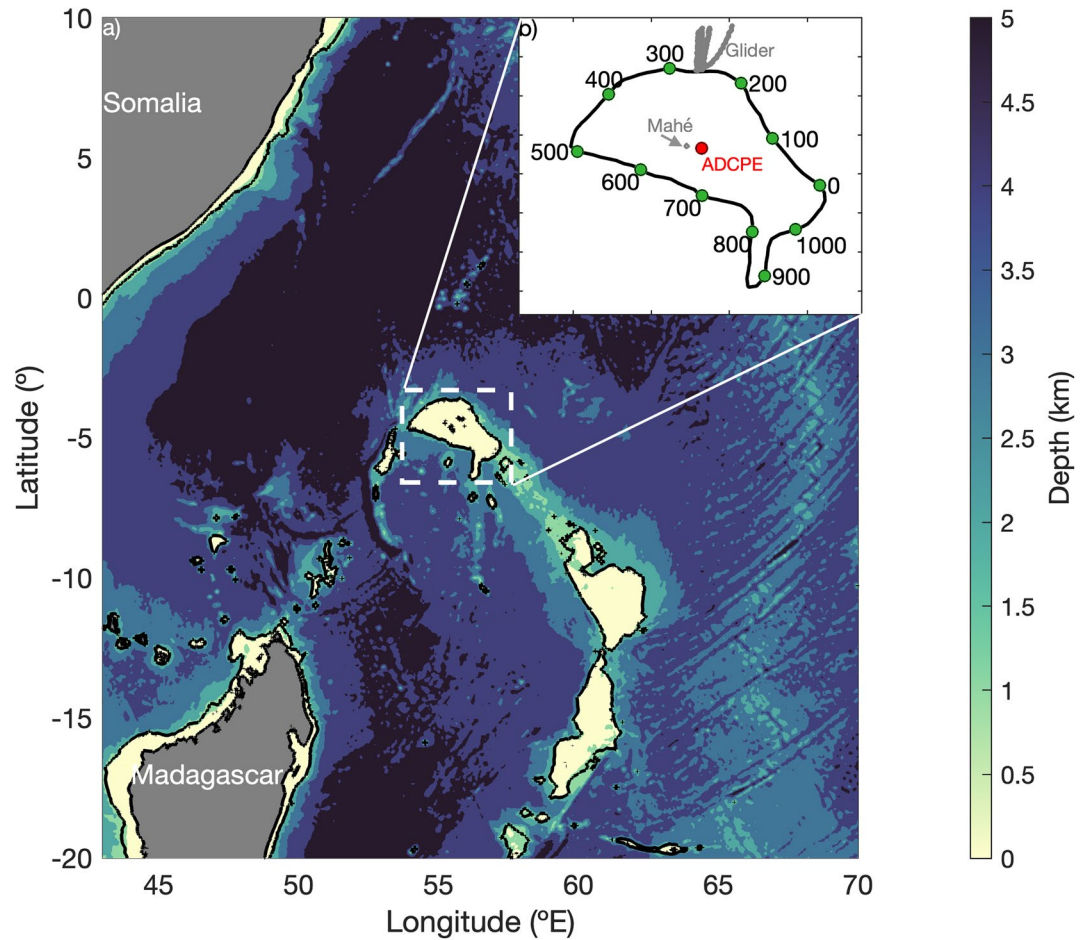


Figure 1. (a) Location of the Seychelles Plateau (enclosed by dashed white lines) in the tropical western Indian Ocean. Bathymetry from the ETOPO1 Global Relief Model is shown in color. Black contours delineate the 0- and 1-km isobaths. Land is shaded in gray. (b) Distance (green dots, in km) from a southeastern point on the POP 1-km isobath (black contour), increasing counterclockwise (i.e., anticyclonically for the Southern Hemisphere) around the plateau. The red dot near the center of the plateau and the gray lines on the northeastern edge of the plateau show the deployment locations of the current velocity meter (ADCPE) and the glider tracks, respectively, discussed in Section 2. Mahé is a small island (~20 km × ~10 km) contoured in gray near the center of the plateau. The insert is ~480 km-wide and ~420 km-long in the x - and y -axis, respectively.

Chatterjee et al., 2013; Miyama et al., 2006; Sengupta et al., 2004) and observations (e.g., Arzeno et al., 2020; Murty et al., 2006; Pujana & McPhaden, 2021) due to their importance in heat flux (Nagura et al., 2014; Smyth et al., 2015), upwelling (Horie et al., 2011; Masumoto et al., 2005; Sengupta et al., 2004), and mixing (Holmes et al., 2016). These waves have periods of ~15 days, wavelengths of ~3700 km (Arzeno et al., 2020), westward phase speeds, and eastward group speeds (per theory). Although Yanai wave energy is strongest in the eastern region of the Indian Ocean (Chatterjee et al., 2013; Miyama et al., 2006), Arzeno et al. (2020) argue that vertical mode-2 Yanai waves are generated westward of the Seychelles Plateau. As previously observed by Sengupta et al. (2004), the Yanai wave energy that reaches the eastern boundary of the Indian Ocean generates coastal-trapped waves, thus prompting our examination of the interaction of Indian Ocean Yanai waves with the Seychelles Plateau.

The goal of this work, carried out as part of the larger North Arabian Sea Circulation autonomous research (NASCar) project (Centurioni et al., 2017) funded by the Office of Naval Research (ONR), is to use the Parallel Ocean Program (POP) numerical model to examine the generation of trapped waves around the Seychelles Plateau by equatorial Yanai waves, driven by observations in both Castillo-Trujillo et al. (2020b) and Arzeno et al. (2020). This paper is organized as follows: in Section 2, we provide information on the POP numerical

model used to study these dynamics, including comparisons with observations. In Sections 3 and 4, we describe the equatorial Yanai wave and trapped wave signatures observed in model output, respectively. In Section 5, we estimate energy fluxes around the Seychelles Plateau. In Section 6, we summarize the findings.

2. POP Model

2.1. Model Description

The results from this study are mainly based on output from an atmospheric reanalysis forced global coupled ocean/sea-ice simulation (McClellan et al., 2018) using CICE4 (Hunke et al., 2010) and the global Los Alamos National Laboratory Parallel Ocean Program Model (POP; Smith et al., 2010), run in the Community Earth System Model (CESM) framework (Hurrell et al., 2013). POP is a primitive equation z -coordinate model; here, it is configured with a nominal 0.1° horizontal grid and 42 depth levels with a vertical resolution that varies from $\Delta z \sim 10$ m at the surface to $\Delta z \sim 250$ m at depth and partial bottom cells (Pacanowski & Gnanadesikan, 1998). Construction of the model bathymetry is described in McClellan et al. (2011). Surface forcing is taken from the Coordinated Ocean-ice Reference Experiment-II corrected interannual forcing (CORE-II CIAF; Large & Yeager, 2004; Large & Yeager, 2009) for 1948–2009. CORE uses 6-hourly National Centers for Environmental Prediction (NCEP) reanalysis for near-surface vector wind, temperature, specific humidity, and density. CORE radiation and precipitation products are from satellite data. Density is calculated from the 25-term equation of state for seawater found in McDougall et al. (2003). Vertical mixing is parameterized using the K -profile parameterization (KPP; Large et al., 1994). Subgridscale horizontal mixing is parameterized using biharmonic operators for momentum and tracers. The values of viscosity and diffusivity vary spatially with the cube of the average grid cell length (Maltrud et al., 1998) and have equatorial coefficient values of $-2.7 \times 10^{10} \text{ m}^4/\text{s}$ and $-0.3 \times 10^{10} \text{ m}^4/\text{s}$ respectively. The model was spun up between 1948 and 1958. There is a free surface, and tides are excluded.

The POP/CICE4 model has been recently used in Palóczy et al. (2020), Palóczy et al. (2018), Wang et al. (2018), and Castillo-Trujillo et al. (2020b). Wang et al. (2018) validated the POP output over the Indian Ocean, north of 5°S , by comparing monthly climatologies of the sea surface height (SSH) field in POP with Archiving, Validation, and Interpretation of Satellite Oceanographic (AVISO) altimetry data, provided by Copernicus Marine Environment Monitoring Service (<http://www.marine.copernicus.eu>). Wang et al. (2018) also compared monthly climatologies of the upper ocean density distribution with the gridded ARGO product (Roemmich & Gilson, 2009). Using both datasets, Wang et al. (2018) saw good agreement between the seasonal cycles of SSH in the altimetry and POP. Castillo-Trujillo et al. (2020b) validated the region of the south-western tropical Indian Ocean by comparing seasonal climatologies of AVISO SSH and geostrophic velocities with those found in the POP model, focused specifically on the Seychelles Plateau. The model showed stronger geostrophic velocities than those derived from AVISO SSH, and there were slight spatial differences in the location of the SSH anomaly zero-crossings; however, there was overall agreement between the model and observations on the seasonal timescale (Castillo-Trujillo et al., 2020b). In Section 2.2, we specifically compare the 10–20 day variance in POP output with instrument and satellite observations.

2.2. Model Validation Against Observations

In this study, we use five years (2005–2009) of daily averaged POP model output consisting of sea surface elevation, wind stress, current velocity, density, and temperature (Arzeno-Soltero et al., 2021). We turn to instrument and satellite data to evaluate the ability of the POP model to resolve dynamics on a 10–20 day timescale. When bandpass-filtering variables, a second-order Butterworth filter is used. Although some of the observations that we reference are not concurrent with the model, we assume that the statistics in both the model and the observations should agree if the dynamics are robust.

Current velocities were measured over the Seychelles Plateau using a 600 kHz RD Instruments acoustic Doppler current profiler (from here on referred to as ADCPE; Figure 1b). ADCPE was bottom-mounted on the 30-m isobath, near the island of Mahé, toward the center of the plateau, and sampled for ~ 30 months

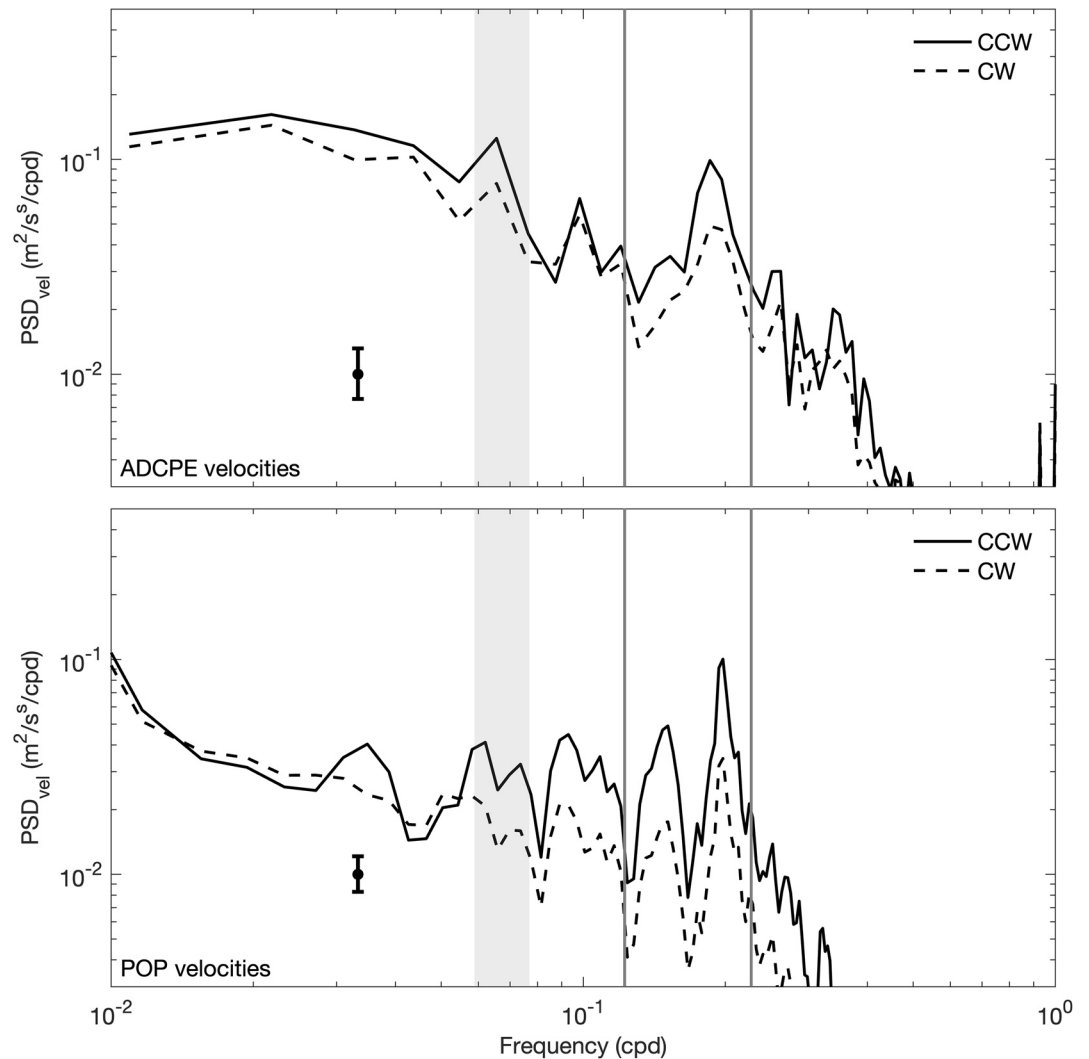


Figure 2. Rotary spectra of depth-averaged ADCPE (top) and POP (bottom) velocities (at the ADCPE location), with 95% confidence intervals. Frequencies corresponding to 13–17 day periods are shaded in gray. The range of inertial frequencies encompassed by the plateau latitudes are shown between the two gray vertical lines.

between 2015 and 2019 (Castillo-Trujillo et al., 2020a, 2020b). The ADCP sampled at 0.5 Hz, resolving profiles in 2 m bins.

ADCPE time series were averaged in 20-min blocks of time, with 50% overlap. When depth-averaged currents were bandpass-filtered to retain 10–20 day variability, their magnitude reached 19 cm/s. For comparison, we extracted daily averaged POP velocities at the same location as the ADCPE site. Depth-averaged bandpass-filtered currents from the POP model are weaker than the ADCPE currents, only reaching magnitudes of up to 7 cm/s. However, both ADCPE and POP rotary spectra show a peak in the spectra in the 13–17 day period band, with energy in the counterclockwise velocity component surpassing the energy in the clockwise velocity component (Figure 2). The spectra are comparable and suggest that the POP model captures a reasonable amount of variance in the 10–20 day period band.

Spectra comparisons were also made between daily averaged POP output and daily delayed-time gridded sea surface heights (SSH) processed by the SL-TAC multimission altimeter data processing system, distributed by the European Copernicus Marine Environment Monitoring Service (Arzeno et al., 2020; CMEMS, 2019; Pujol et al., 2016). Data for these comparisons were extracted from two locations near the plateau and one location in the equatorial Indian Ocean, based on areas where the 10–20 day bandpass-filtered POP SSH

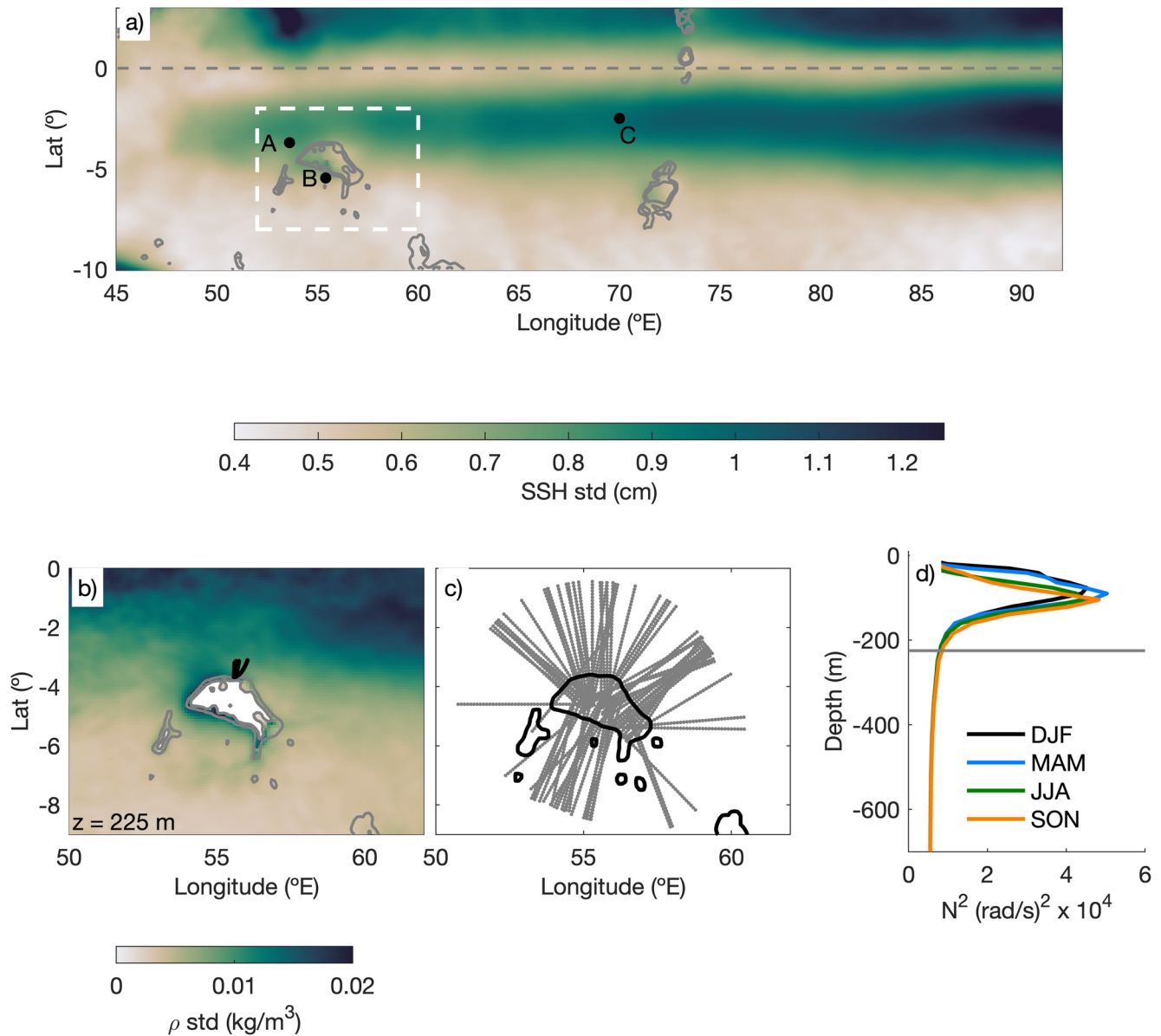


Figure 3. Standard deviation for POP model 10–20 day bandpass-filtered (a) sea surface height (SSH) and (b) density at 225 m. The 0-m, 200-m, and 1-km contours are outlined in solid gray. The equator is demarcated by a dashed gray line. The three black dots in (a) correspond to locations in Figure 4. The solid black lines in (b) correspond to the glider path (data shown in Figure 5). (c) Cross-sections used to estimate N^2 in (d) according to Appendix A. The dashed white square in (a) encloses the area shown in (b) and (c). The solid gray line in (d) marks $z = -150$ m.

exhibited elevated variance (Figure 3a). Spectra from both the POP model output and the altimeter data show similar elevated levels of energy in the 10–20 day band across the three locations (Figure 4), suggesting that the POP model reproduces quasi-biweekly variance in the near-equatorial region.

Elevated variance is also seen near the northern and western edges of the Seychelles Plateau in the 10–20 day bandpass-filtered density output from the POP model (Figure 3b). To provide more context, we present stratification profiles (where buoyancy frequency is defined as $N^2 = -(g / \rho_0) \partial \rho / \partial z$, with $\rho_0 = 1026$ kg/m³) estimated on cross-sections around the plateau (Figure 3c; Appendix A). Following Castillo-Trujillo et al. (2020b), we divided and averaged our N^2 profiles into four seasons: December–February (DJF), March–May (MAM), June–August (JJA), and September–November (SON). Profiles were also averaged radially and among the cross-sections. Overall, $6.5 \times 10^{-3} < N < 2.0 \times 10^{-2}$ rad/s; and seasonal changes in

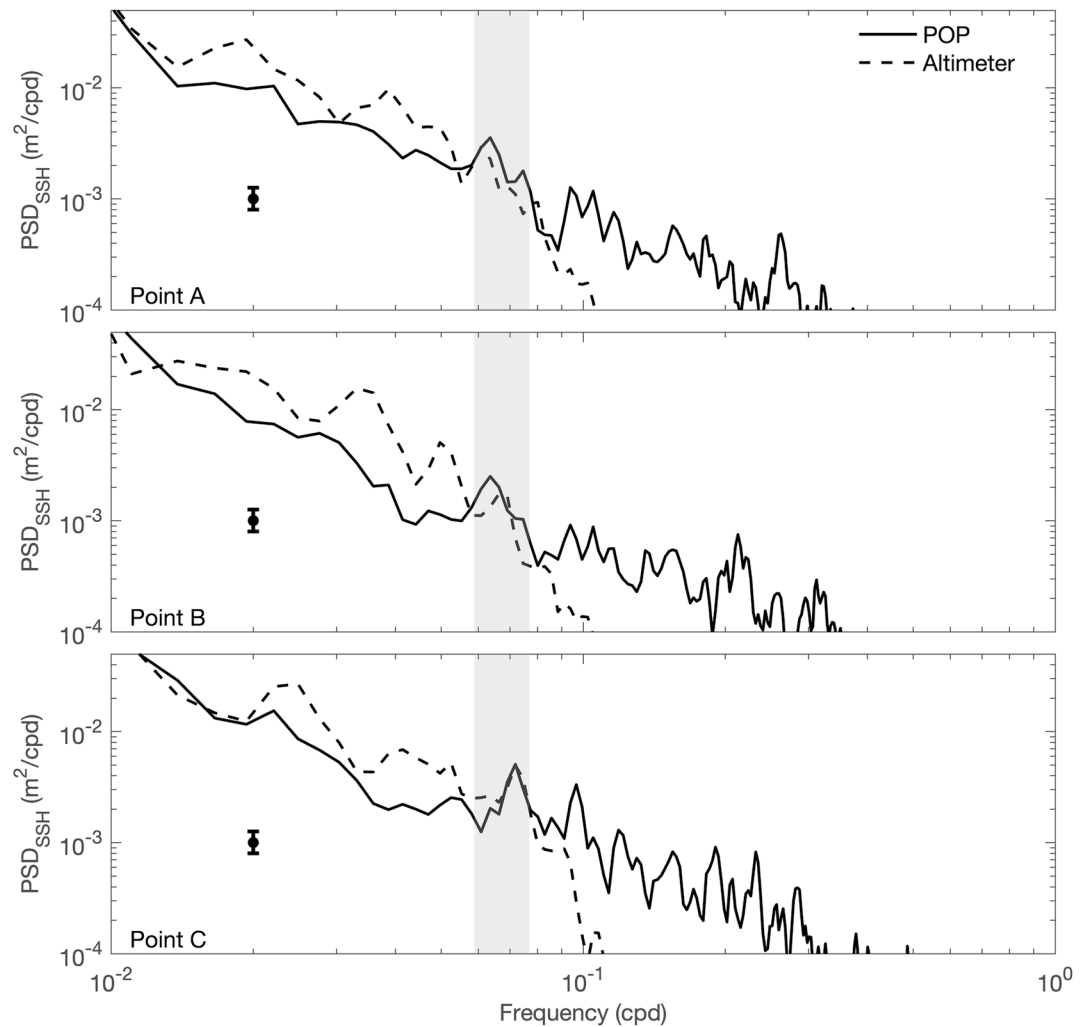


Figure 4. Spectra of sea surface displacement from POP model output and altimeter data for the three points in Figure 3 (top), with 95% confidence intervals. Frequencies corresponding to 13–17 day periods are shaded in gray.

stratification are mainly reflected in the depth of maximum N^2 , varying between 75 m (DJF) and 105 m (SON; Figure 3d). The standard deviations presented in Figure 3b, at 225 m, are below the pycnocline, but the water column is quite stratified at that depth ($N \sim 9 \times 10^{-3}$ rad/s), limiting vertical motions. The Burger number (S ; Equation 1) can be estimated using the depth-median value of the four average stratification profiles ($N \sim 7 \times 10^{-3}$ rad/s Figure 3d), $H / L_H = 0.05$ (the plateau slope), and the f range across the plateau (8.9×10^{-6} rad/s $< |f| < 1.7 \times 10^{-5}$ rad/s). Taking this into consideration, the Burger number for the Seychelles Plateau is $460 < S < 1600$. Given that the Burger number is a ratio of the Rossby radius of deformation (L_R) to a plateau cross-sectional length scale (L_H ; Equation 1), a large S such as this suggests that the waves trapped around the Seychelles Plateau resemble internal Kelvin waves and “see” the plateau as a vertical wall (Huthnance, 1978; Rhines, 1970).

Additional observations were gathered by an autonomous underwater glider that sampled the upper 1,000 m at the edge of the Seychelles Plateau from January to March 2018 (Rainville & Lee, 2019). This Seaglider occupied 15 meridional sections extending from the plateau edge near 3.7°S to about 60 km offshore, near 3.1°S (Figures 1b and 3b). Temperature and salinity, measured in a vertical saw-tooth pattern from the surface to a 1-km depth (with an average 1.7 km distance between profiles), are used to estimate isopycnal displacements (ζ) relative to the 3-month average density section.

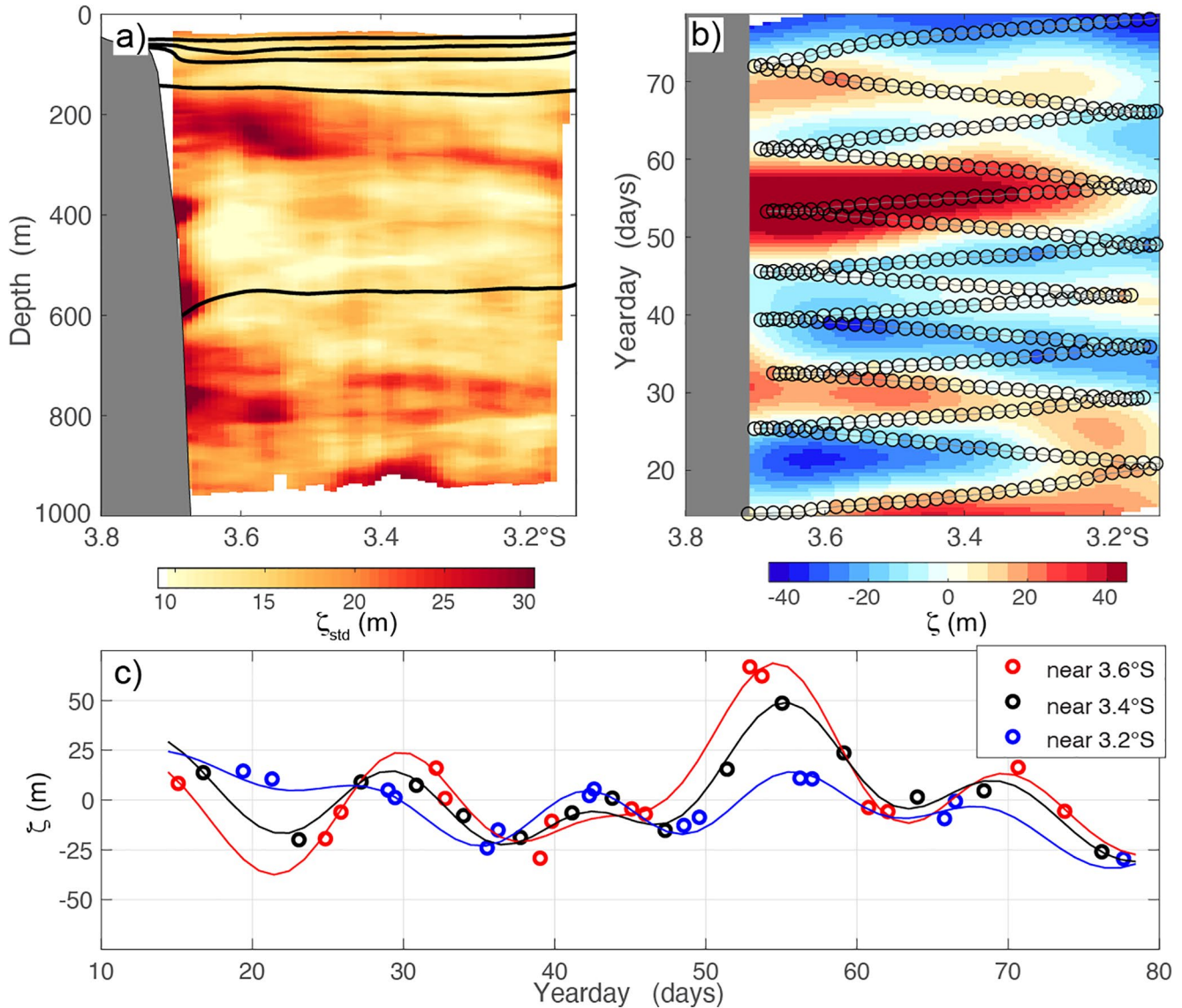


Figure 5. (a) Standard deviation of isopycnal displacements (ζ) estimated from the 15 Seaglider sections in Figure 1. Potential density contours for $\rho_\theta = 1023, 1024, 1025, 1026,$ and 1027 kg/m^3 are depicted in black. (b) Isopycnal displacement as a function of latitude and time, averaged between 200 and 250 m. Circles show the glider estimates (along the gray path), and the background is an objective map with decorrelation scales of 10 days and 60 km, selected to be consistent with the signal in ADCPE, though the map is not overly sensitive to the choice of these scales. (c) Time series of isopycnal displacement at 3.6°S (red), 3.4°S (black), and 3.2°S (blue). Glider estimates (circles) and objective map (lines) are shown.

The standard deviation of ζ , relative to the spatial mean of the 15 glider sections, shows enhanced amplitude close to the plateau, with magnitudes decaying offshore (Figure 5), suggesting the presence of dynamics that are trapped to the plateau slope. The decrease in amplitude as a function of distance (latitude) is most obvious between 200–250 m. From repeat transects, displacement at this depth indicates oscillations with a period of 12–15 days (Figures 5b and 5c). While gliders have long endurance (this glider subsequently transited to the Maldives, 2,000 km away), they transit slowly. Each line took about 5 days to complete, with uneven sampling at each latitude (Figures 5b and 5c), which limits our ability to constrain the periodicity and structure of the oscillatory signal. Despite these limitations, it is apparent that the signal at periods of around 2 weeks dominates the variance during these 3 months, and that the amplitude of the signal is enhanced closer to the plateau edge. Although we cannot accurately compare the glider variance directly to the model due to differences in spatial resolution between both types of data, the glider observations support the existence of quasi-biweekly elevated density variance (Figure 3b) close to the plateau edge.

3. Yanai Wave

We first take a look at the quasi-biweekly equatorial Yanai wave signature in the POP model. The Yanai wave signature is mainly described in terms of antisymmetric sea level anomalies (ASLA) across the equator:

$$ASLA = \frac{1}{2}(SLA_n - SLA_s), \quad (3)$$

where SLA_n and SLA_s are sea level anomalies averaged meridionally between $2 - 3^\circ\text{N}$ and $2 - 3^\circ\text{S}$, respectively (Yanai & Murakami, 1970). Composite maps were formed to compare the Yanai wave signal in the POP model output with the Yanai wave signal in satellite observations presented in Arzeno et al. (2020).

Composites of Yanai wave propagation (Figure 6) include POP sea surface height (SSH) and wind velocities. The wind velocities are derived from POP model wind stresses, following Equation 1 of Appendix A in Delman et al. (2018). Each composite (Figures 6b–6g) was constructed following the methods in Arzeno et al. (2020) by averaging the 10–20 day bandpass-filtered time series at each available grid point using a time series $\Theta_Y(t)$ to determine the averaging intervals, where the subscript Y stands for “Yanai.”

Following Arzeno et al. (2020), $\Theta_Y(t)$ is defined using a Hilbert Empirical Orthogonal Function (HEOF) analysis of 10–20 day bandpass-filtered ASLA. Similar to Empirical Orthogonal Functions (EOFs), HEOFs decompose a signal into spatial and temporal components:

$$\chi(x, t) = \sum_j \Theta_j(t) \gamma_j^*(x), \quad (4)$$

where $\Theta(t)$ is a complex temporal amplitude, $\gamma(x)$ is a complex spatial amplitude, $(*)$ represents the complex conjugate, and j is an orthogonal mode number. Unlike with regular EOFs, HEOFs use the Hilbert transform (a phase shift of the original signal by $-\pi/2$) to allow us to capture wave-like structures in scalar time series.

The first and second HEOF modes capture 45% and 26% of the variance of the model ASLA, respectively, similar to the results in Arzeno et al. (2020) using satellite data (37% and 25% for mode 1 and mode 2, respectively). Given that the first HEOF mode (Figure 6a) captures the highest percentage of the variance, we define $\Theta_Y(t)$ as the amplitude time series of this mode, which is assumed to be representative of the Yanai wave (i.e., $\Theta_Y(t) = \Theta_1(t)$ when $\chi(x, t)$ is the ASLA). Similar to the satellite composites in Arzeno et al. (2020), the phase averaged composites using POP output (Figures 6b–6g) show the Yanai wave SSH phase progressing westward, as expected from theory, while the wind velocities form structures akin to westward-propagating vortices (Chen & Chen, 1993). The Yanai wave SSH signal is seen to extend as far west as the Seychelles Plateau, as noted in Arzeno et al. (2020). The composite amplitudes are notably lower in the western basin, a concept discussed in Sengupta et al. (2004) as eastern intensification. Wavelengths were determined using the results from the spatial modal decomposition; periods were estimated by applying spectral analysis to the amplitude time series. The Yanai wavelength and period at 2.5°S were $\lambda = 4500 \text{ km} \pm 0.2 \text{ km}$, and $T = 13.4 \pm 0.2 \text{ days}$, respectively, resulting in a phase speed of $c = -3.9 \text{ m/s} \pm 0.5 \text{ m/s}$. Although, on average, the model composite wavelength (period) is longer (shorter) than that found in satellite data, the average phase speed of the Yanai wave in the POP model output is comparable to that found using satellite data ($\lambda \sim 4100 \text{ km}$, $T \sim 14 \text{ days}$, $c \sim -3.4 \text{ m/s}$; Arzeno et al., 2020). This improves our confidence that the POP model is adequately capturing the quasi-biweekly Yanai wave signal.

4. Trapped Wave

Here we shift our attention to the Seychelles Plateau, demarcated by the 1-km isobath inside the box in Figure 1a. Virtual moorings extracted along the 1-km isobath are used to show properties as a function of distance around the plateau (see the 1-km isobath in Figure 1b). Time series extracted from the virtual mooring locations refer to spatial averages over $\sim 60 \text{ km} \times \sim 30 \text{ km}$ areas centered on each of the virtual mooring coordinates, where the 60 and 30 km segments cover, roughly, the along-isobath and offshore directions. Unless otherwise noted, the model output presented in this manuscript from here on is bandpass-filtered to include variations with periods between 10–20 days, in order to capture dynamics of the quasi-biweekly Yanai wave in the tropical Indian Ocean.

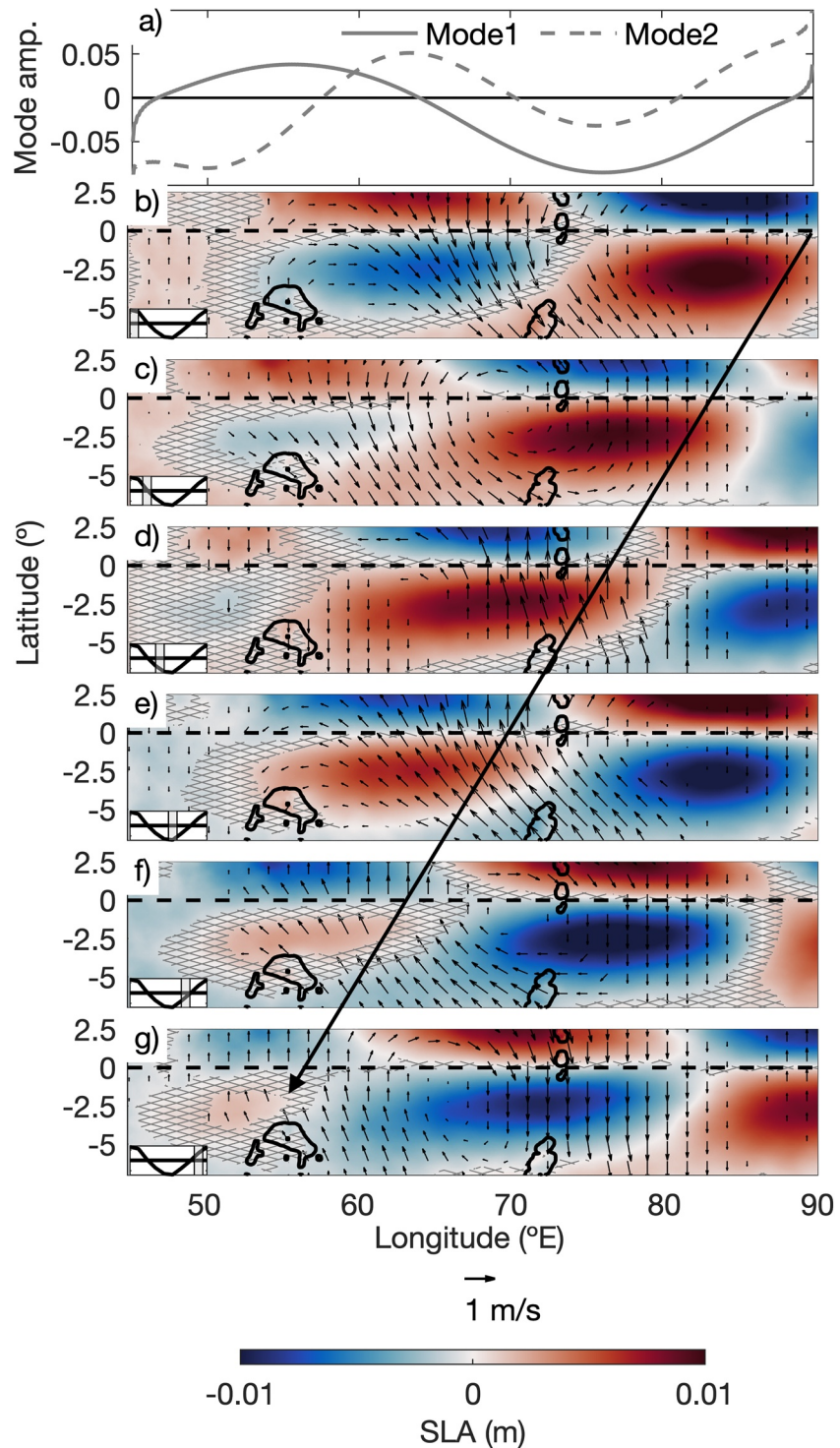


Figure 6. (a) Real part of the spatial amplitude pertaining to the first ASLA HEOF modes. (b–g) Phase averages of 10–20 day bandpass-filtered POP SSH output (color) and wind velocities (vectors). Averages were obtained following the phase of Θ_γ , as described in Section 3 and Arzeno et al. (2020). The insets show the average ASLA cycle (solid line) and the phase represented in each subplot (shaded area). The hatching denotes areas where SSH phase averages are not statistically different from zero for a p-value of 0.05. The arrow across b–g traces the propagation of a node throughout a cycle. Contours delineate the 0- and 1- km isobaths, from the POP model bathymetry.

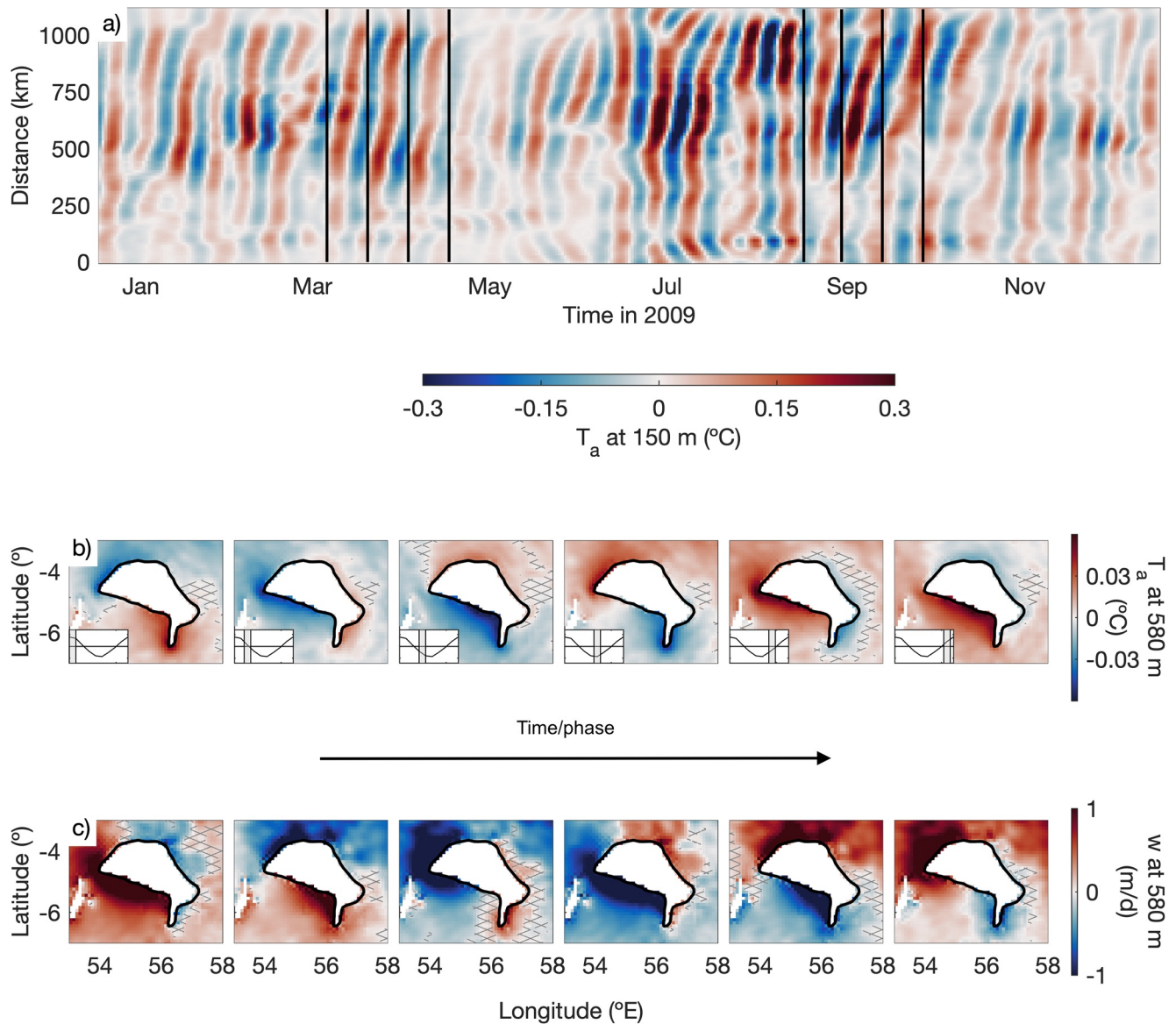


Figure 7. (a) Hovmöller diagram of 10–20-day bandpass-filtered temperature anomalies (T_a) at 150 m, taken over the 1-km isobath. The time series shown spans 1 year out of our 5-year model output. Distances around the plateau are depicted in Figure 1b, where 0 indicates the southeast point. Black vertical lines are plotted to indicate 14-day time intervals as a reference for the reader. (b–c) Composites of 10–20 day temperature anomalies (b) and vertical velocities (c) at $z = 580$ m, created using Θ_p . Shaded areas denote regions where the mean is not significantly different from zero for a p-value of 0.05. Insets in row (b) mark the phase of Θ_p corresponding to each column.

Temperature time series at 150 m along the virtual mooring locations show periods of oscillations generally propagating anticyclonically around the Seychelles Plateau (Figure 7a), interspersed with periods where oscillations seem to impact all moorings simultaneously. The maximum and minimum temperature anomalies at this depth are 0.66°C and -0.71°C , respectively, corresponding to vertical displacements of 17 m and -18 m, respectively. However, the average temperature anomaly magnitude and its standard deviation was 0.16°C , corresponding to a vertical displacement of 4 m. To further study the dominant characteristics of these oscillations, HEOF analysis was applied to the density time series at the virtual mooring locations.

HEOFs were first calculated for each individual depth, assuming that each layer acts independently of the others. This is useful for understanding at what depth the trapped wave signal might be the strongest and most coherent. At all depths below 120 m the first HEOF mode captures over 50% of the variance in the

10–20 day band, reaching greater than 70% of the variance between $z \sim 450$ m and $z \sim 800$ m. At all depths below 120 m, the first density HEOF mode has the spatial structure of an azimuthal wavenumber 1 wave, with positive and negative anomalies on opposite sides of the plateau. Above 120 m depth, the signal breaks down and represents less of the variance, likely due to upper ocean processes dominating the variance in the mixed layer.

As a result, we focus further analyses at depths below 120 m, repeating the HEOF decomposition using all depths below 120 m in a single decomposition. Doing so, the HEOF analysis can (a) allow wave-like structures that are propagating across depths and (b) construct a single amplitude time series to capture the propagation of a wave along the Seychelles Plateau in the 10–20 day band, rather than creating separate amplitude time series for each depth. When the HEOF decomposition includes all depths below 120 m in a single analysis, the first HEOF mode captures 42% of the variance; the amplitude time series for the first HEOF mode ($\Theta_P(t)$, where the subscript P represents the plateau) has bulk and peak periods of 15 and 16 days, respectively ($\omega = 4.8 \times 10^{-6}$ rad/s and $\omega = 4.5 \times 10^{-6}$ rad/s, respectively). The Coriolis parameter changes across the plateau (8.9×10^{-6} rad/s $< |f| < 1.7 \times 10^{-5}$ rad/s), but the trapped wave frequency is always around $0.5|f|$ or less. Because Θ_P has the spatial structure of a wave with an azimuthal wavenumber 1, we take the wavelength of the trapped wave to be $\gamma \sim 1000$ km, the approximate plateau circumference. This leads to an estimate of the phase speed of the wave traveling around the Seychelles Plateau of $c_P \sim 0.75$ m/s.

Composites of temperature and vertical velocity around the Seychelles Plateau were created using $\Theta_P(t)$, the amplitude time series for the first HEOF mode (resulting from the HEOF analysis that examined all depths below 120 m simultaneously) to determine the averaging intervals (Figures 7b and 7c). At 580 m, where the previous depth-varying HEOF analysis captured over 70% of the density variance in its first mode, the trapped wave signature clearly propagates anticyclonically (counterclockwise in the Southern Hemisphere) around the plateau. Although the temperature anomalies at this depth are small (their magnitude reaches up to 0.08°C, since this depth is well below the pycnocline; Figure 3d) the vertical velocity is comparable to the equatorial upwelling in the Pacific (Johnson et al., 2001) and the monthly upwelling induced by Ekman pumping around the plateau (Yokoi et al., 2008), which has been linked to elevated chlorophyll patterns (Dilmahamod et al., 2016; Resplandy et al., 2009).

The amplitude time series representative of the Yanai wave ($\Theta_Y(t)$) and the oscillations around the plateau ($\Theta_P(t)$) have a maximum amplitude correlation of $|-0.51| \pm 0.07$ (where the negative indicates an inverse correlation and the error bounds are 95% confidence intervals) when $\Theta_P(t)$ lags $\Theta_Y(t)$ by 5 days, emphasizing the relationship between the plateau-trapped wave $\Theta_P(t)$ and the Yanai wave $\Theta_Y(t)$. In other words, while the Yanai wave and the trapped wave may not always be in-phase, they are linked; changes in the Yanai wave will affect changes in the plateau-trapped wave within about a third of a wave period.

5. Energy Flux

In order to map energy pathways near the Seychelles Plateau, we turn to estimates of energy flux density. Energy flux is a useful measure to identify energy sources and sinks in a region, as well as quantify the amount of energy that is potentially available for mixing and dissipation. We discuss energy flux estimates in the 10–20 day period band in their full form, not decomposed into their barotropic and baroclinic components, to account for changes in bathymetry along the Seychelles Plateau slope (Musgrave, 2019). However, when we look at the baroclinic energy flux by itself, the results are very similar, suggesting that trapped waves around the Seychelles Plateau propagate as if they are on a flat bottom along a vertical wall, akin to Kelvin waves, given the steep plateau edges.

Energy flux (F) is defined as:

$$F_i = \langle u'_i p' \rangle, \quad (5)$$

where u'_i and p' are the full velocity and pressure perturbations at a certain depth, respectively, i denotes the horizontal velocity component (zonal, meridional), and $\langle \rangle$ represents a mean over a wave period. The pressure perturbations are deduced from a vertical integral of density anomalies associated with the wave and defined as

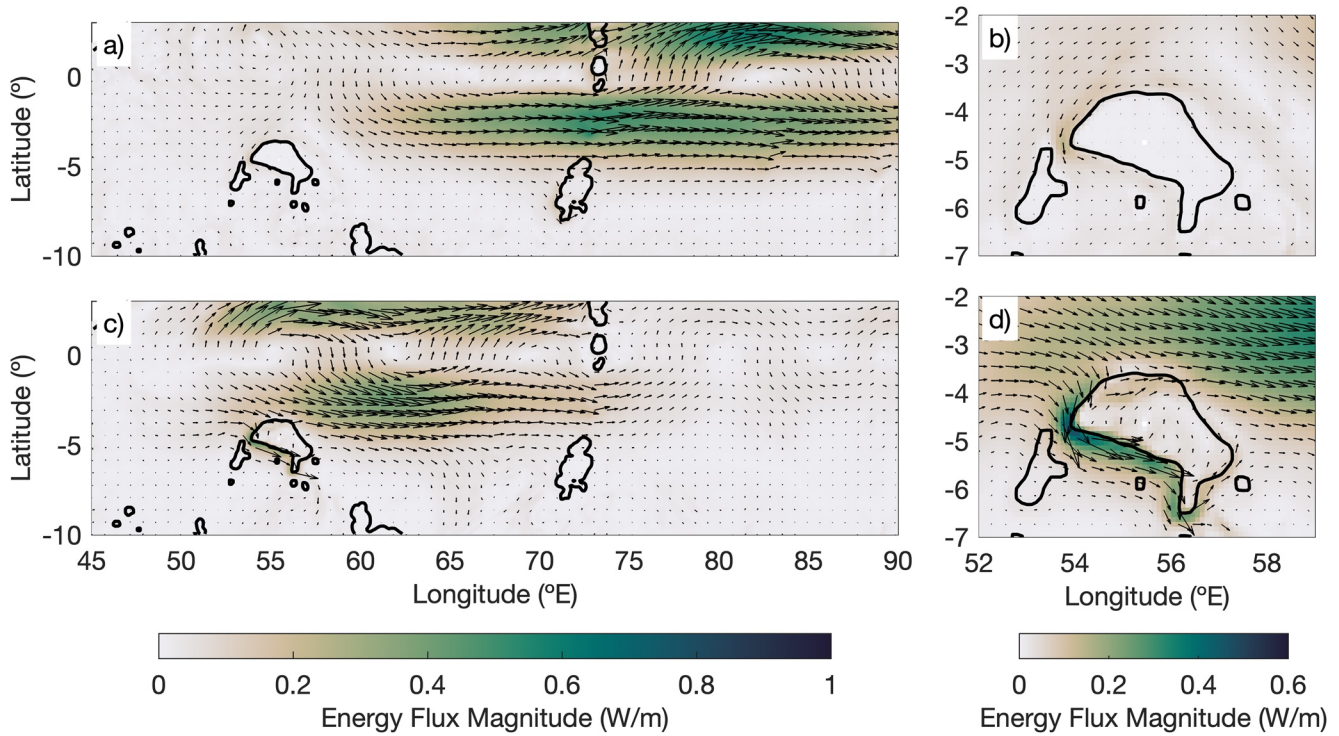


Figure 8. Depth-integrated horizontal energy flux (F) estimated from phase averages using (a and b) $\Theta_Y(t)$ or (c and d) $\Theta_P(t)$. Black contours delineate the 1-km POP isobath.

$$p'(x, y, z, t) = \frac{g}{\rho_0} \int_z^{\eta} \rho'(x, y, z^*, t) dz^*, \quad (6)$$

where the primes denote perturbations associated with the wave, η is a sea surface displacement, and $\rho_0 = 1026 \text{ kg/m}^3$. Wave-related perturbations are represented using 10–20 day bandpass-filtered phase averaged variables. Phase averages were conducted as described in Sections 3 and 4, using $\Theta_Y(t)$ or $\Theta_P(t)$ to determine the phases. Conservative upper and lower bounds were computed for energy flux estimates, as described in Appendix B.

Depth-integrated fluxes—resulting from variables averaged using $\Theta_Y(t)$ and $\Theta_P(t)$ (Figures 8a and 8c, respectively)—are eastward near the equator, evocative of the Yanai wave SSH signal (Figure 6), and agreeing with theory (quasi-biweekly Yanai wave energy flux opposes the phase propagation). The magnitude of the horizontal energy flux differs if $\Theta_Y(t)$ or $\Theta_P(t)$ are used to define the averaging intervals: $F(x, y)$ estimated using $\Theta_Y(t)$ shows consistent magnitudes above $F \sim 0.2 \text{ W/m}$ eastward of 65° E . If $\Theta_P(t)$ is used, $F > 0.2 \text{ W/m}$ between $\sim 55^\circ \text{ E}$ and $\sim 65^\circ \text{ E}$, with decaying magnitudes to the east. The similar spatial patterns, as well as previous work by Arzeno et al. (2020) that suggests Yanai wave generation by quasi-biweekly wind fluctuations occurs as far west as 50° E , imply that both phase definitions (Figures 8a and 8c) capture the same Yanai wave structure, with differing magnitudes highlighting different regions of the same spatially varying wave. From here on, the velocities, pressure perturbations, and energy fluxes discussed will refer to those estimated from phase averages using $\Theta_P(t)$, which highlight the structure of the trapped wave near the plateau.

An enlarged view of the Seychelles Plateau (Figure 8d) shows anticyclonic energy flux, with the largest magnitudes around the western and southern sides of the plateau. The energy around the Seychelles Plateau appears connected to the energy from the quasi-biweekly Yanai wave, given that the depth-integrated energy flux estimates that flank the southern side of the equator near the 55° E longitude (pertaining to the Yanai wave), deviate and point into the north-western side of the plateau. The depth-integrated energy

flux on the eastern side of the Seychelles Plateau appears to be diminished and dominated by the opposite-signed flux from the quasi-biweekly Yanai wave.

To better understand the energy flux around the plateau, we separate F into azimuthal and radial components (F_θ, F_r), where the azimuthal is defined using the angle of the 1-km isobath. The azimuthal energy flux is positive counterclockwise (the direction of trapped wave propagation), and radial energy flux is positive if energy is coming into the plateau (right-handed coordinate system). Azimuthal and radial energy fluxes were extracted from the virtual moorings on the 1-km isobath (see Figure 1b), spatially averaged over a $\sim 60 \text{ km} \times \sim 30 \text{ km}$ area.

The depth-integrated azimuthal energy flux is either positive or near zero around most of the plateau (Figures 9a and 9c, with distances specified in Figure 1b), suggesting that energy is propagating anticyclonically, as is expected from a trapped wave and consistent with the depth-integrated picture in Figure 8. The depth-varying azimuthal energy flux shows consistently positive values deeper than $\sim 100 - 150 \text{ m}$ depth, while positive and negative surface-intensified azimuthal energy fluxes (significantly different from zero) are seen in the top 100 m of the water column (Figure 9e). We conclude that quasi-biweekly Yanai waves are the source of this enhanced flux, given that (a) they have similar periods to the plateau-trapped waves and (b) previous work shows that Yanai wave energy is stronger near the surface than deeper in the water column (Miyama et al., 2006). Since Yanai wave energy flux is eastward, it is projected (near the surface) on the plateau as counterclockwise (positive) and clockwise (negative) energy flux from 500–800 km and 0–500 km, respectively. Aside from the top 100 m of the water column, segments with positive azimuthal energy fluxes that are significantly different from zero are located in the north, north-western, and south-western flanks ($\sim 350 - 800 \text{ km}$, between S1 and S2; Figure 9e); the signal dampens as the wave progresses to the south-eastern region of the Seychelles Plateau (from S2 to S3).

Similar to azimuthal energy fluxes, radial energy fluxes (Figures 9b–9f) show that most of the energy is injected into the plateau region over the top 100 m, particularly along the north-western, western, and south-western flanks of the plateau. Based on the fluxes shown in Figure 8, we could attribute this surface-intensified flux to the Yanai wave (between S1 and S2). Aside from the top 100 m of the water column, the only regions with significant radial energy flux are at the plateau outcrop, between S2 and S3 ($\sim 800 \text{ km}$). With the exception of the outcrop, most of the energy flux below 100 m (radial and azimuthal) is, statistically, non-distinct from zero.

To further look at energy flux profiles, energy flux values were extracted along four sets of POP cross-sections spaced $\sim 250 \text{ km}$ apart (Figures 9a and 9b). These four cross-sections were chosen to avoid areas where the bathymetry surfaces above a 1-km depth, while still capturing the relatively shallower bathymetry on the southeastern side of the plateau (S3). Each set of azimuthal velocities is obtained by averaging over five cross-sections covering a distance of 50 km in the along-isobath direction. Azimuthal energy flux along the four sets of cross-sections in Figure 9a shows the trapped wave signal propagating counterclockwise (positive F_θ) around the plateau (Figure 10). The Yanai wave signal is highlighted in both F_θ and F_r . The F_θ contribution from the Yanai wave appears as a negative (clockwise) surface-intensified signal (over the top 100 m) in S1 and S4 due to the projection of the Yanai wave onto the plateau. Some of the positive surface-intensified F_θ in S2 can also be attributed to the passing Yanai wave. The F_r contribution from the Yanai wave appears as a positive (into the plateau) surface-intensified signal in S1 and S2 and as a negative (out of the plateau) surface-intensified signal in S4. The trapped wave signal is weak at both S3 and S4; much of the signal is not statistically different from zero (Figure 10).

To understand how much energy could be available for mixing and dissipation in the plateau system, we estimate the total azimuthal energy flux attributed to the trapped wave at each cross-section by vertically and radially integrating F_θ over the locations where the value is statistically different from zero (defined as having error bounds that do not cross zero). Across the four cross-sections, the total positive azimuthal energy flux ranged from $F_\theta^T = 0.06 \text{ kW}$ to $F_\theta^T = 31.0 \text{ kW}$ (Table 1), with the highest values occurring at S1 and S2. The decrease in azimuthal energy flux between S2 and S3 suggests that wave scattering and dissipation may play an important role as the wave encounters changes in plateau geometry (e.g., the outcrop between S2 and S3; Figure 9a) and bathymetry (see shallower depths near S3 in Figure 1a) on the southern flank (Wilkin & Chapman, 1990). The integrated radial energy flux (integrated in depth and distance along the plateau edge) contained large error bounds, so a proper value was not attained.

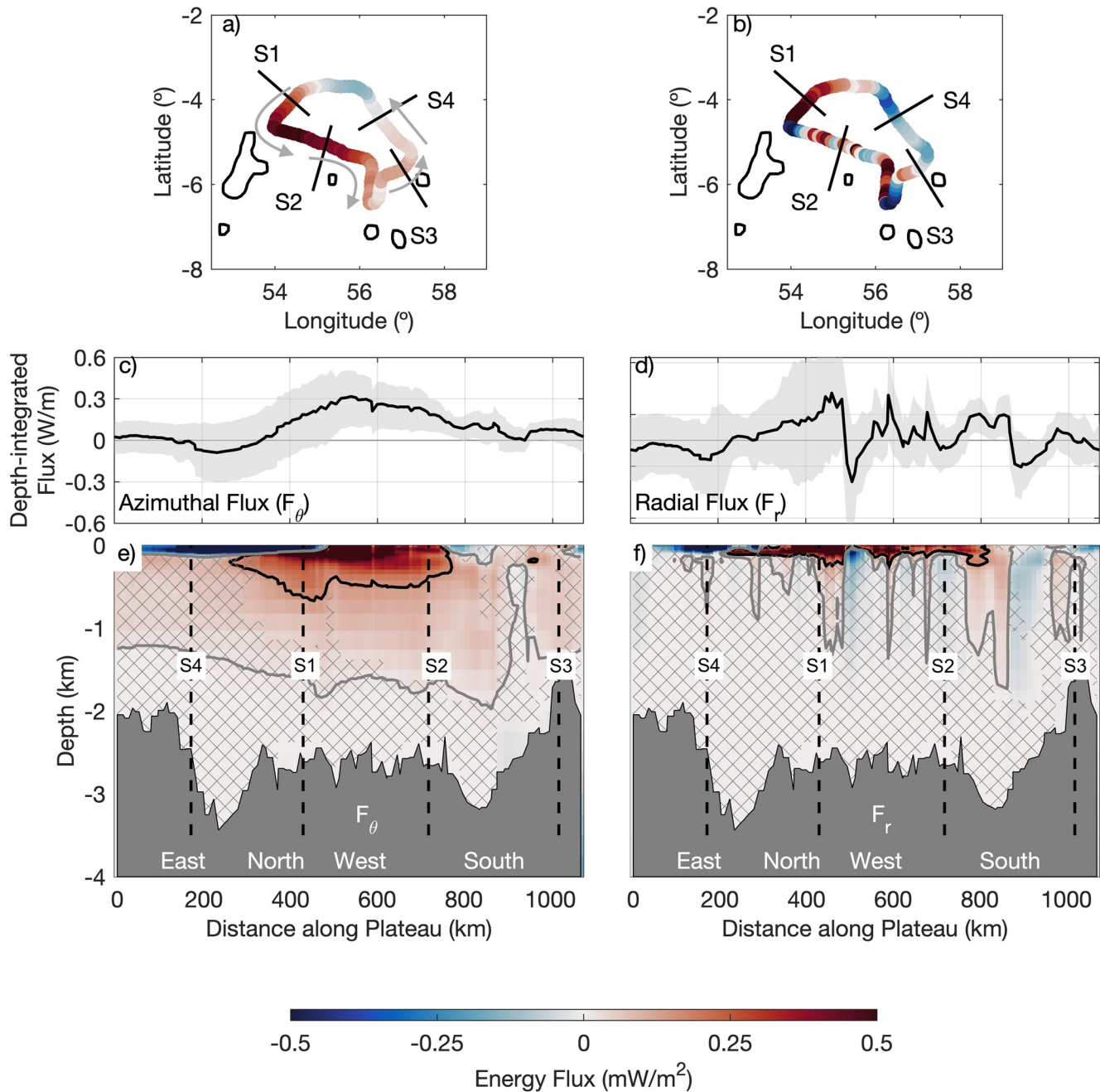


Figure 9. Azimuthal (left: a, c, and e) and radial (right: b, d, and f) energy flux around the Seychelles Plateau integrated over the water column (a–d) and as a function of depth (e and f), with distance around the plateau 1-km isobath as depicted in Figure 1b. Gray arrows in (a) suggest the general propagation of the trapped wave. General cardinal directions appear near the bottom to orient the reader. The black and gray contours mark $F = 0.15 \text{ mW/m}^2$ and $F = 0.015 \text{ mW/m}^2$, respectively. The gray hatching denotes the areas where the energy flux is not statistically different from zero. Solid black lines in (a) and (b) and dashed black lines in (e and f) depict the approximate locations of the four sets of cross-sections shown in Figure 10.

It should be noted that all of our estimates of F_θ and F_r depend on having captured the correct cross-sectional structure of the trapped wave, since these are referenced to the angle of the 1-km isobath. The positive F_r below $\sim 500 \text{ m}$ shown in Figure 9f could, for example, be an artifact of an incorrect rotation. Nonetheless, Figures 9 and 10 taken together suggest that the trapped wave is a mechanism by which energy input into the system by Yanai waves in the upper water column gets redistributed vertically around some region of

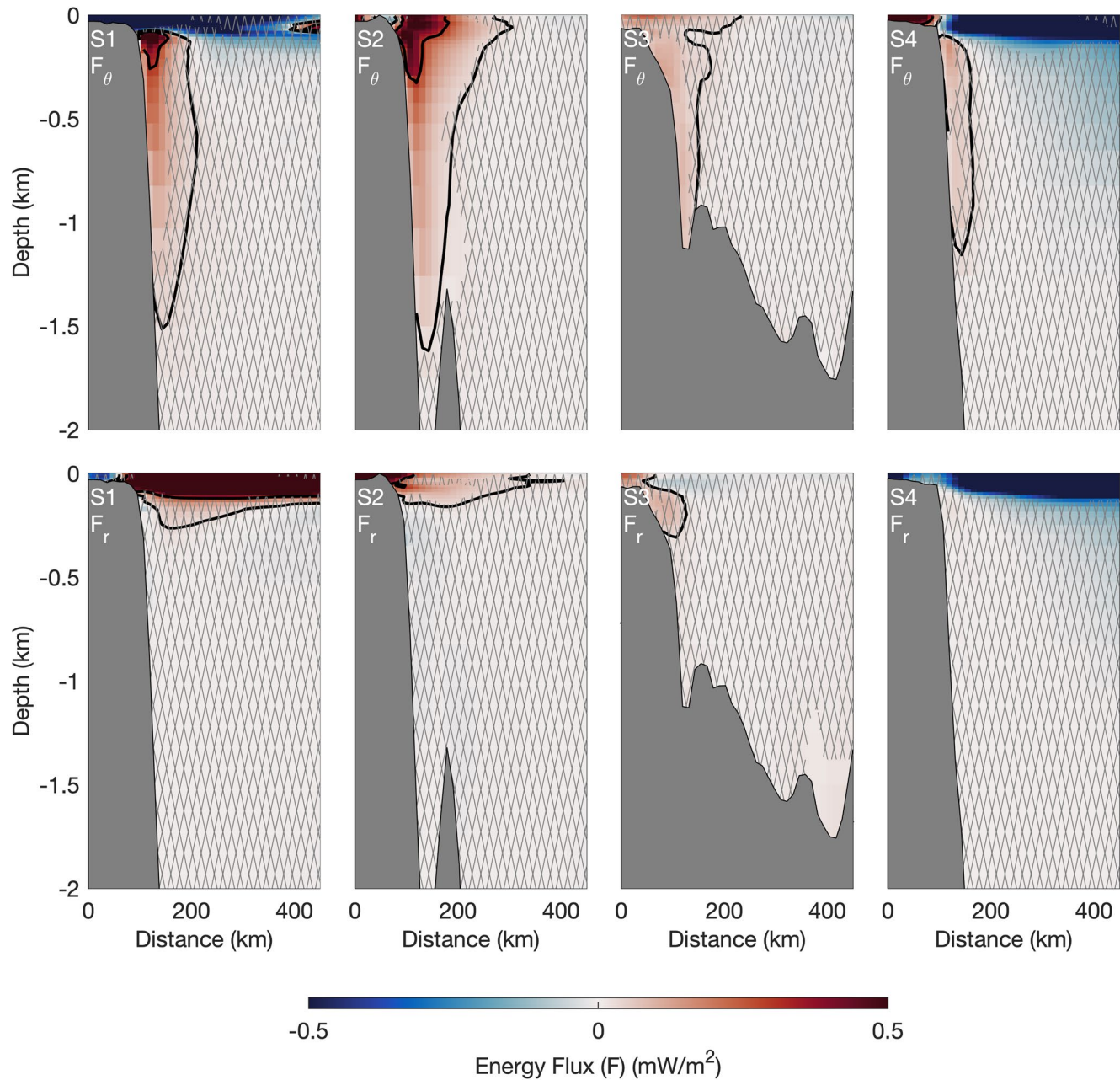


Figure 10. Azimuthal (top) and radial (bottom) energy flux across the four cross-section sets in Figure 8. Each set consists of five individual cross-sections, which we average. Positive F_θ is counterclockwise around the plateau. The black contour marks $F_\theta = 0.015 \text{ mW/m}^2$. The gray hatching denotes the areas where the energy flux is not statistically different from zero.

the plateau. Moreover, the integrated F_θ values in Table 1 provide a general sense of the energy that could be available for mixing and dissipation in the plateau system.

6. Summary

Previous studies on seamount dynamics have focused on regions outside of the tropics, where Burger numbers are relatively small and trapped waves can be excited by tidal currents (e.g., Brink, 1995; Codiga & Eriksen, 1997; Hunkins, 1986). This study examines trapped waves around the Seychelles Plateau, located in the tropical Indian Ocean, a low-latitude, high Burger number ($S > 400$) environment.

Table 1
Depth-Integrated Energy Flux (kW)

Section	Lower bound ^a	Mean	Upper bound ^a
F_{θ} Section 1	1.7	11.1	25.1
F_{θ} Section 2	7.0	18.1	31.0
F_{θ} Section 3	0.6	5.7	15.0
F_{θ} Section 4	0.06	1.7	5.5
F_R^b	-120.0	13.0	147.1

^aUpper and lower bounds are conservative error estimates (Appendix B). ^bIntegrated along entire plateau circumference.

Our research is motivated by instrument and satellite data, as well as model output in the equatorial Indian Ocean. Current velocities on the Seychelles Plateau show energy in the 10–40 day band (Castillo-Trujillo et al., 2020b) and, more specifically, in the 10–20 day band (Figure 2). Energy at similar periods is found in satellite data. In particular, Arzeno et al. (2020) argue that quasi-biweekly Yanai waves (periods ~ 14 days) with eastward propagating energy are generated west of the Seychelles Plateau by quasi-biweekly vortex-like winds based on satellite SSH, suggesting that these could interact with the Seychelles Plateau, much like Rossby waves generate coastal-trapped Kelvin waves. Similarly, output from the POP model highlights enhanced 10–20 day variance near the equator and around the plateau (Figures 3a and 3b). Glider data suggests that elevated isopycnal displacement variance is strongest close to the plateau slope and decays offshore, with isopycnals oscillating at 10–20 day periods. Given this combination of factors, we used the POP model to study quasi-biweekly dynamics around the Seychelles Plateau and their connection to equatorial Yanai waves.

We identified the signature of both quasi-biweekly Yanai waves and plateau-trapped waves in POP model output using phase averages and HEOF analysis. The HEOF amplitude time series allowed us to estimate a significant correlation (~0.5) between both the Yanai wave and the trapped wave. Furthermore, we identified that trapped waves around the Seychelles Plateau have significant vertical velocities associated with their propagation (Figure 7), which can influence ecological productivity through upwelling and mixing, raising the nutricline and allowing nutrients to be entrained in the mixed layer. These dynamics could thus, contribute to the elevated primary productivity present around the Seychelles Plateau (George et al., 2018; Yokoi et al., 2008).

We estimated energy fluxes around the Seychelles Plateau to get a sense of the amount of energy available for mixing and dissipation in the region, as well as to relate the energy around the Seychelles Plateau to potential sources and sinks. Exploring the role of plateau-trapped waves in the energy pathway is particularly relevant considering that equatorial regions are noted to have low dissipation and diapycnal diffusivity rates (Gregg et al., 2003; Kunze et al., 2006). Around the Seychelles Plateau, the azimuthal energy flux (F_{θ}) varies between 0.06 and 31.0 kW, or up to $F_{\theta} \sim 0.3$ W/m. The largest divergence in energy flux occurs between the cross-sections S2 and S3 (Figure 9), as the trapped wave rounds the outcrop on the southern section of the plateau and encounters shallower bathymetry (e.g., see Figure 1), pointing to a potential site of wave scattering (Wilkin & Chapman, 1990) and dissipation. The depth-integrated horizontal energy fluxes suggest that quasi-biweekly Yanai waves play a role in the energy flux around the Seychelles Plateau (Figure 8). Cross-sections of energy fluxes around the plateau note that the Yanai wave influence on the plateau is surface-intensified, limited to the upper ~ 100 m of the water column, while the trapped wave redistributes that energy vertically across depths and around the plateau. Yanai waves may also be exciting trapped waves around other bathymetric features in the equatorial Indian Ocean such as the Chagos Ridge, where Sengupta et al. (2004) observe elevated quasi-biweekly energy in their model's horizontal velocity. We also see quasi-biweekly upwelling and downwelling patterns around the Chagos Ridge, similar to those around the Seychelles Plateau (Figure 7), but this is not the focus of our work. This work puts forth the need

for further measurements in the tropical Indian Ocean to explore the interactions between planetary waves and seamounts near the equatorial waveguide.

Appendix A: Cross-Sections

Each cross-section that contributes to the N^2 profiles in Figure 3d is normal to the POP model's 1-km contour and extends a distance inwards equal to the plateau radius (r_p). We choose $r_p = 160$ km, consistent with the approximate Seychelles Plateau 1-km isobath circumference. We extracted a total of 129 cross-sections from POP (each cross-section is 5–15 km apart, covering the entire 1 km contour); however, about half of those cross-sections were eliminated from consideration, due to locally complex bathymetry. For example, we eliminated cross-sections with bathymetry that was never deeper than 3.5 km or cross-sections that intersected shallow protrusions (another island or seamount). In the end, we include 80 cross-sections (Figure 3c) in our averages.

Appendix B: Energy Flux Error Analysis

Phase averages of bandpass-filtered density, sea surface height, and velocity were ascribed a standard error equivalent to $\sigma_E = \frac{\sigma}{\sqrt{N}}$, where σ_E is the standard error, σ is the standard deviation, and N is the effective degrees of freedom. Given that the variables in the energy flux estimate (Equation 5) are not independent, we cannot use the standard error propagation formula to carry forth the uncertainty. Instead, upper and lower bounds on any variable F (representing density, sea surface height, and velocity) are defined as $F \pm \sigma_E$. All further calculations are done with the mean variables F and their respective upper and lower bounds. For example, while the mean energy flux is estimated as

$$F_i = \langle u'_i p' \rangle, \quad (\text{B1})$$

the lower bound of the energy flux will be the minimum value of the following 4 equations:

$$F_i = \langle (u'_i - \sigma_{uE})(p' - \sigma_{pE}) \rangle, \quad (\text{B2})$$

$$F_i = \langle (u'_i - \sigma_{uE})(p' + \sigma_{pE}) \rangle, \quad (\text{B3})$$

$$F_i = \langle (u'_i + \sigma_{uE})(p' + \sigma_{pE}) \rangle, \quad (\text{B4})$$

$$F_i = \langle (u'_i + \sigma_{uE})(p' - \sigma_{pE}) \rangle, \quad (\text{B5})$$

where σ_{uE} and σ_{pE} are the standard error of the velocity and the pressure, respectively. While this may render overly conservative error bounds, it is the most appropriate approach for the propagation of error in a nonlinear system.

Data Availability Statement

ADCP current velocity data and POP model output are posted online as part of the UC San Diego Library Digital Collections ([doi:10.6075/J0ZS2V1M](https://doi.org/10.6075/J0ZS2V1M) and [doi:10.6075/J0XW4HCF](https://doi.org/10.6075/J0XW4HCF), respectively). Publicly available satellite data from the E.U. Copernicus Marine Environment Monitoring Service (CMEMS, 2019) can be found at http://marine.copernicus.eu/services-portfolio/access-to-products/?option=com_csw&view=details&product_id=SEALEVEL_GLO_PHY_L4_REP_OBSERVATIONS_008_047. Glider data is posted online as part of the University of Washington's ResearchWorks Archive (<http://hdl.handle.net/1773/46967>).

Acknowledgments

Support for the field study and for Arzeno-Soltero, Giddings and Pawlak was provided by the Office of Naval Research (ONR) under the NASCar DRI (Terri Paluszkiwicz and Scott Harper), awards N00014-15-1-2319 to Giddings and N00014-15-1-2303 to Pawlak. McClean and Wang were supported by ONR grant N00014-15-1-2189 to McClean. Julie McClean was also supported by U.S. Department of Energy (DOE) grants SC0012778 and SC0020073. Rainville and Lee were funded by ONR grant N00014-15-1-2296. Funding for the POP/CICE simulation was provided by a DOE BER grant entitled "Ultra High Resolution Global Climate Simulation" via a Los Alamos National Laboratory subcontract (to McClean); Caroline Papadopoulos (SIO/UCSD) and Elena Yuleva (UCSD) carried out the POP/CICE simulation. The POP simulation used Yellowstone (ark:/85065/d7wd3xhc) computational resources provided by the National Center for Atmospheric Research (NCAR)'s Climate Simulation Laboratory (CSL), sponsored by the National Science Foundation (NSF). Isabella B. Arzeno-Soltero has been funded through the National Defense Science & Engineering Graduate Fellowship (NDSEG) Program, as well as the Ford Foundation Dissertation Fellowship. Operational support in the Seychelles was provided by the Better Life Foundation, and additional logistical support was provided by Robert Ashton. We extend our gratitude to the Seychelles Fishing Authority, the Seychelles Meteorological Authority, and the Seychelles Coast Guard for field support and valuable discussions. Ralph Tirant and Eric Morel provided the small boat operations. Robert Todd, Richard Walsh, Lillian McCormick, Mohammad Sedarat, Beverly French, Katelin Pedersen, André Amador, Madeleine Harvey, Hugo Sánchez Ulloa, Larry George, Alfredo Girón Nava, Ben Jokinen, and Robert Grenzeback are gratefully acknowledged for their help with field work. The authors would also like to acknowledge Ken Brink (WHOI) for allowing us the use of his idealized model, which is not included in this paper but was valuable for developing our understanding of these trapped waves. We also thank the two anonymous reviewers who greatly improved this manuscript with their insightful feedback.

References

Arzeno, I. B., Giddings, S. N., Pawlak, G., & Pinkel, R. (2020). Generation of quasi-biweekly Yanai waves in the equatorial Indian Ocean. *Geophysical Research Letters*, 47(16), e2020GL088915. <https://doi.org/10.1029/2020GL088915>

Arzeno-Soltero, I. B., Giddings, S. N., Pawlak, G., McClean, J. L., & Wang, H. (2021). *Daily POP model output over the equatorial Indian Ocean*. UC San Diego Library Digital Collections. <https://doi.org/10.6075/J0XW4HCF>

Brink, K. (1982). A comparison of long coastal trapped wave theory with observations off Peru. *Journal of Physical Oceanography*, 12(8), 897–913. [https://doi.org/10.1175/1520-0485\(1982\)012<0897:acolct>2.0.co;2](https://doi.org/10.1175/1520-0485(1982)012<0897:acolct>2.0.co;2)

Brink, K. (1989). The effect of stratification on seamount-trapped waves. *Deep Sea Research Part I: Oceanographic Research Papers*, 36(6), 825–844. [https://doi.org/10.1016/0198-0149\(89\)90031-9](https://doi.org/10.1016/0198-0149(89)90031-9)

Brink, K. (1990). On the generation of seamount-trapped waves. *Deep Sea Research Part I: Oceanographic Research Papers*, 37(10), 1569–1582. [https://doi.org/10.1016/0198-0149\(90\)90062-Z](https://doi.org/10.1016/0198-0149(90)90062-Z)

Brink, K. (1995). Tidal and lower frequency currents above Fieberling Guyot. *Journal of Geophysical Research: Oceans*, 100(C6), 10817–10832. <https://doi.org/10.1029/95JC00998>

Castillo-Trujillo, A. C., Arzeno, I. B., Giddings, S. N., Pawlak, G., McClean, J., & Rainville, L. (2020a). *Data from: Observations and modeling of ocean circulation in the Seychelles plateau region*. UC San Diego Library Digital Collections. <https://doi.org/10.6075/J0ZS2V1M>

Castillo-Trujillo, A. C., Arzeno, I. B., Giddings, S. N., Pawlak, G., McClean, J. L., & Rainville, L. (2020b). Observations and modeling of ocean circulation in the Seychelles Plateau region. *Journal of Geophysical Research: Oceans*, 126, e2020JC016593. <https://doi.org/10.1029/2020JC016593>

Centurioni, L. R., Hormann, V., Talley, L. D., Arzeno, I., Beal, L., Caruso, M., et al. (2017). Northern Arabian Sea Circulation-autonomous research (NASCar): A research initiative based on autonomous sensors. *Oceanography*, 30(2), 74–87. <https://doi.org/10.5670/oceanog.2017.224>

Chapman, D. C. (1989). Enhanced subinertial diurnal tides over isolated topographic features. *Deep Sea Research Part I: Oceanographic Research Papers*, 36(6), 815–824. [https://doi.org/10.1016/0198-0149\(89\)90030-7](https://doi.org/10.1016/0198-0149(89)90030-7)

Chapman, D. C., & Haidvogel, D. B. (1992). Formation of Taylor caps over a tall isolated seamount in a stratified ocean. *Geophysical & Astrophysical Fluid Dynamics*, 64(1–4), 31–65. <https://doi.org/10.1080/03091929208228084>

Chatterjee, A., Shankar, D., McCreary, J., & Vinayachandran, P. (2013). Yanai waves in the western equatorial Indian Ocean. *Journal of Geophysical Research: Oceans*, 118(3), 1556–1570. <https://doi.org/10.1002/jgrc.20121>

Chelton, D. B., DeSzoeke, R. A., Schlax, M. G., El Naggar, K., & Siwertz, N. (1998). Geographical variability of the first baroclinic Rossby radius of deformation. *Journal of Physical Oceanography*, 28(3), 433–460. [https://doi.org/10.1175/1520-0485\(1998\)028<0433:gvotfb>2.0.co;2](https://doi.org/10.1175/1520-0485(1998)028<0433:gvotfb>2.0.co;2)

Chen, T.-C., & Chen, J.-M. (1993). The 10–20-day mode of the 1979 Indian monsoon: Its relation with the time variation of monsoon rainfall. *Monthly Weather Review*, 121(9), 2465–2482. [https://doi.org/10.1175/1520-0493\(1993\)121<2465:tdmoti>2.0.co;2](https://doi.org/10.1175/1520-0493(1993)121<2465:tdmoti>2.0.co;2)

Clark, M. R., Rowden, A. A., Schlacher, T., Williams, A., Consalvey, M., Stocks, K. I., et al. (2010). The ecology of seamounts: Structure, function, and human impacts. *Annual Review of Marine Science*, 2, 253–278. <https://doi.org/10.1146/annurev-marine-120308-081109>

CMEMS. (2019). *Global ocean gridded L4 sea surface heights and derived variables reprocessed (1993-ongoing)*. Retrieved from http://marine.copernicus.eu/services-portfollio/access-to-products/?option=com_csw&view=details&product_id=SEALEVEL_GLO_PHY_L4_REP_OBSERVATIONS_008_047

Codiga, D. L. (1997). Physics and observational signatures of free, forced, and frictional stratified seamount-trapped waves. *Journal of Geophysical Research*, 102(C10), 23009–23024. <https://doi.org/10.1029/97JC01452>

Codiga, D. L., & Eriksen, C. C. (1997). Observations of low-frequency circulation and amplified subinertial tidal currents at Cobb Seamount. *Journal of Geophysical Research*, 102(C10), 22993–23007. <https://doi.org/10.1029/97JC01451>

Delman, A. S., McClean, J. L., Sprintall, J., Talley, L. D., & Bryan, F. O. (2018). Process-specific contributions to anomalous Java mixed layer cooling during positive IOD events. *Journal of Geophysical Research: Oceans*, 123(6), 4153–4176. <https://doi.org/10.1029/2017JC013749>

Dilmahamad, A., Hermes, J., & Reason, C. (2016). Chlorophyll-a variability in the Seychelles-Chagos thermocline ridge: Analysis of a coupled biophysical model. *Journal of Marine Systems*, 154, 220–232. <https://doi.org/10.1016/j.jmarsys.2015.10.011>

Dower, J., Freeland, H., & Juniper, K. (1992). A strong biological response to oceanic flow past Cobb Seamount. *Deep Sea Research Part I: Oceanographic Research Papers*, 39(7–8), 1139–1145. [https://doi.org/10.1016/0198-0149\(92\)90061-W](https://doi.org/10.1016/0198-0149(92)90061-W)

Egbert, G. D., & Ray, R. D. (2003). Semi-diurnal and diurnal tidal dissipation from TOPEX/Poseidon altimetry. *Geophysical Research Letters*, 30(17). <https://doi.org/10.1029/2003GL017676>

George, J. V., Nuncio, M., Anilkumar, N., Chacko, R., & Rajashekhar, D. (2018). Seasonal surface chlorophyll-a variability in the Seychelles–Chagos thermocline ridge. *Current Science*, 114(4), 868. <https://doi.org/10.18520/cs/v114/404/868-878>

Goldner, D. R., & Chapman, D. C. (1997). Flow and particle motion induced above a tall seamount by steady and tidal background currents. *Deep Sea Research Part I: Oceanographic Research Papers*, 44(5), 719–744. [https://doi.org/10.1016/S0967-0637\(96\)00131-8](https://doi.org/10.1016/S0967-0637(96)00131-8)

Gregg, M. C., Sanford, T. B., & Winkel, D. P. (2003). Reduced mixing from the breaking of internal waves in equatorial waters. *Nature*, 422(6931), 513–515. <https://doi.org/10.1038/nature01507>

Haidvogel, D. B., Beckmann, A., Chapman, D. C., & Lin, R.-Q. (1993). Numerical simulation of flow around a tall isolated seamount. Part II: Resonant generation of trapped waves. *Journal of Physical Oceanography*, 23(11), 2373–2391. [https://doi.org/10.1175/1520-0485\(1993\)023<2373:nsosfaa>2.0.co;2](https://doi.org/10.1175/1520-0485(1993)023<2373:nsosfaa>2.0.co;2)

Holmes, R., Moum, J., & Thomas, L. N. (2016). Evidence for seafloor-intensified mixing by surface-generated equatorial waves. *Geophysical Research Letters*, 43(3), 1202–1210. <https://doi.org/10.1002/2015GL066472>

Horii, T., Masumoto, Y., Ueki, I., Kumar, S. P., & Mizuno, K. (2011). Intraseasonal vertical velocity variation caused by the equatorial wave in the central equatorial Indian Ocean. *Journal of Geophysical Research*, 116(C9). <https://doi.org/10.1029/2011JC007081>

Hunke, E. C., Lipscomb, W. H., Turner, A. K., Jeffery, N., & Elliott, S. (2010). *CICE: The Los Alamos sea ice model documentation and software user's manual version 4.1 la-cc-06-012* (Vol. 675, p. 500). T-3 Fluid Dynamics Group, Los Alamos National Laboratory.

Hunkins, K. (1986). Anomalous diurnal tidal currents on the Yermak Plateau. *Journal of Marine Research*, 44(1), 51–69. <https://doi.org/10.1357/002224086788460139>

Hurrell, J. W., Holland, M. M., Gent, P. R., Ghan, S., Kay, J. E., Kushner, P. J., et al. (2013). The Community Earth System Model: A framework for collaborative research. *Bulletin of the American Meteorological Society*, 94(9), 1339–1360. <https://doi.org/10.1175/BAMS-D-12-00121.1>

Huthnance, J. M. (1978). On coastal trapped waves: Analysis and numerical calculation by inverse iteration. *Journal of Physical Oceanography*, 8(1), 74–92. [https://doi.org/10.1175/1520-0485\(1978\)008<0074:OCTWAA>2.0.CO;2](https://doi.org/10.1175/1520-0485(1978)008<0074:OCTWAA>2.0.CO;2)

- Johnson, G. C., McPhaden, M. J., & Firing, E. (2001). Equatorial Pacific Ocean horizontal velocity, divergence, and upwelling. *Journal of Physical Oceanography*, 31(3), 839–849. [https://doi.org/10.1175/1520-0485\(2001\)031<0839:EPOHVD>2.0.CO;2](https://doi.org/10.1175/1520-0485(2001)031<0839:EPOHVD>2.0.CO;2)
- Kunze, E., Firing, E., Hummon, J. M., Chereskin, T. K., & Thurnherr, A. M. (2006). Global abyssal mixing inferred from lowered ADCP shear and CTD strain profiles. *Journal of Physical Oceanography*, 36(8), 1553–1576. <https://doi.org/10.1175/JPO2926.1>
- Large, W. G., McWilliams, J. C., & Doney, S. C. (1994). Oceanic vertical mixing: A review and a model with a nonlocal boundary layer parameterization. *Reviews of Geophysics*, 32(4), 363–403. <https://doi.org/10.1029/94RG01872>
- Large, W. G., & Yeager, S. G. (2004). *Diurnal to decadal global forcing for ocean and sea-ice models: The data sets and flux climatologies*. University Corporation for Atmospheric Research.
- Large, W. G., & Yeager, S. G. (2009). The global climatology of an interannually varying air–sea flux data set. *Climate Dynamics*, 33(2–3), 341–364. <https://doi.org/10.1007/s00382-008-0441-3>
- Lavelle, J. W., & Mohn, C. (2010). Motion, commotion, and biophysical connections at deep ocean seamounts. *Oceanography*, 23(1), 90–103. <https://doi.org/10.5670/oceanog.2010.64>
- Lueck, R. G., & Mudge, T. D. (1997). Topographically induced mixing around a shallow seamount. *Science*, 276(5320), 1831–1833. <https://doi.org/10.1126/science.276.5320.1831>
- Maltrud, M. E., Smith, R. D., Semtner, A. J., & Malone, R. C. (1998). Global eddy-resolving ocean simulations driven by 1985–1995 atmospheric winds. *Journal of Geophysical Research*, 103(C13), 30825–30853. <https://doi.org/10.1029/1998JC900013>
- Masumoto, Y., Hase, H., Kuroda, Y., Matsuura, H., & Takeuchi, K. (2005). Intraseasonal variability in the upper layer currents observed in the eastern equatorial Indian Ocean. *Geophysical Research Letters*, 32(2). <https://doi.org/10.1029/2004GL021896>
- McClean, J. L., Bader, D. C., Bryan, F. O., Maltrud, M. E., Dennis, J. M., Mirin, A. A., et al. (2011). A prototype two-decade fully-coupled fine-resolution CCSM simulation. *Ocean Modelling*, 39(1–2), 10–30. <https://doi.org/10.1016/j.ocemod.2011.02.011>
- McClean, J. L., Bader, D. C., Maltrud, M. E., Evans, K. J., Taylor, M., Tang, Q., et al. (2018). High-resolution fully-coupled acme v0.1 approximate present day transient climate simulations. In 2018 Ocean Sciences Meeting.
- McDougall, T. J., Jackett, D. R., Wright, D. G., & Feistel, R. (2003). Accurate and computationally efficient algorithms for potential temperature and density of seawater. *Journal of Atmospheric and Oceanic Technology*, 20(5), 730–741. [https://doi.org/10.1175/1520-0426\(2003\)20<730:ACEAF>2.0.CO;2](https://doi.org/10.1175/1520-0426(2003)20<730:ACEAF>2.0.CO;2)
- Miyama, T., McCreary, J. P., Sengupta, D., & Senan, R. (2006). Dynamics of biweekly oscillations in the equatorial Indian Ocean. *Journal of Physical Oceanography*, 36(5), 827–846. <https://doi.org/10.1175/JPO2897.1>
- Morato, T., Hoyle, S. D., Allain, V., & Nicol, S. J. (2010). Seamounts are hotspots of pelagic biodiversity in the open ocean. *Proceedings of the National Academy of Sciences*, 107(21), 9707–9711. <https://doi.org/10.1073/pnas.0910290107>
- Mullineau, L. S., & Mills, S. W. (1997). A test of the larval retention hypothesis in seamount-generated flows. *Deep Sea Research Part I: Oceanographic Research Papers*, 44(5), 745–770. [https://doi.org/10.1016/S0967-0637\(96\)00130-6](https://doi.org/10.1016/S0967-0637(96)00130-6)
- Murty, V., Sarma, M., Suryanarayana, A., Sengupta, D., Unnikrishnan, A., Fernando, V., et al. (2006). *Indian moorings: Deep-sea current meter moorings in the eastern equatorial Indian Ocean*. (Vol. 11). CLIVAR Exchanges.
- Musgrave, R. (2019). Energy fluxes in coastal trapped waves. *Journal of Physical Oceanography*, 49(12), 3061–3068. <https://doi.org/10.1175/JPO-D-18-0172.1>
- Nagura, M., Masumoto, Y., & Horii, T. (2014). Meridional heat advection due to mixed Rossby-gravity waves in the equatorial Indian Ocean. *Journal of Physical Oceanography*, 44(1), 343–358. <https://doi.org/10.1175/JPO-D-13-0141.1>
- Pacanowski, R. C., & Gnanadesikan, A. (1998). Transient response in a z-level ocean model that resolves topography with partial cells. *Monthly Weather Review*, 126(12), 3248–3270. [https://doi.org/10.1175/1520-0493\(1998\)126<3248:TRIAZL>2.0.CO;2](https://doi.org/10.1175/1520-0493(1998)126<3248:TRIAZL>2.0.CO;2)
- Palóczy, A., Gille, S. T., & McClean, J. L. (2018). Oceanic heat delivery to the Antarctic continental shelf: Large-scale, low-frequency variability. *Journal of Geophysical Research: Oceans*, 123(11), 7678–7701. <https://doi.org/10.1029/2018JC014345>
- Palóczy, A., McClean, J. L., Gille, S. T., & Wang, H. (2020). The large-scale vorticity balance of the Antarctic continental margin in a fine-resolution global simulation. *Journal of Physical Oceanography*, 50(8), 2173–2188. <https://doi.org/10.1175/JPO-D-19-0307.1>
- Pujiana, K., & McPhaden, M. J. (2021). Biweekly mixed Rossby-gravity waves in the equatorial Indian Ocean. *Journal of Geophysical Research: Oceans*, 126(5), e2020JC016840. <https://doi.org/10.1029/2020JC016840>
- Pujol, M.-I., Faugère, Y., Taburet, G., Dupuy, S., Pelloquin, C., Ablain, M., & Picot, N. (2016). DUACS DT2014: The new multi-mission altimeter data set reprocessed over 20 years. *Ocean Science*, 12(5), 1067–1090. <https://doi.org/10.5194/os-12-1067-2016>
- Rainville, L., & Lee, C. (2019). *Seaglider data from SG128 near the Seychelles, 2018. Data to accompany the article "Generation of low-latitude seamount-trapped waves: A case study of the Seychelles Plateau," by Arzeno-Soltero et al. Journal of Geophysical Research - Oceans, 2021.* Retrieved from <http://hdl.handle.net/1773/46967>
- Resplandy, L., Vialard, J., Lévy, M., Aumont, O., & Dandonneau, Y. (2009). Seasonal and intraseasonal biogeochemical variability in the thermocline ridge of the southern tropical Indian Ocean. *Journal of Geophysical Research*, 114(C7). <https://doi.org/10.1029/2008JC005246>
- Rhines, P. (1970). Edge-, bottom-, and Rossby waves in a rotating stratified fluid. *Geophysical & Astrophysical Fluid Dynamics*, 1(3–4), 273–302. <https://doi.org/10.1080/03091927009365776>
- Roemmich, D., & Gilson, J. (2009). The 2004–2008 mean and annual cycle of temperature, salinity, and steric height in the global ocean from the Argo program. *Progress in Oceanography*, 52(2), 81–100. <https://doi.org/10.1016/j.pocean.2009.03.004>
- Rowden, A. A., Dower, J. F., Schlacher, T. A., Consalvey, M., & Clark, M. R. (2010a). Paradigms in seamount ecology: Fact, fiction and future. *Marine Ecology*, 31, 226–241. <https://doi.org/10.1111/j.1439-0485.2010.00400.x>
- Rowden, A. A., Schlacher, T. A., Williams, A., Clark, M. R., Stewart, R., Althaus, F., et al. (2010b). A test of the seamount oasis hypothesis: Seamounts support higher epibenthic megafaunal biomass than adjacent slopes. *Marine Ecology*, 31, 95–106. <https://doi.org/10.1111/j.1439-0485.2010.00369.x>
- Schott, F. A., & McCreary, J. P., Jr (2001). The monsoon circulation of the Indian Ocean. *Progress in Oceanography*, 51(1), 1–123. [https://doi.org/10.1016/S0079-6611\(01\)00083-0](https://doi.org/10.1016/S0079-6611(01)00083-0)
- Schott, F. A., Xie, S.-P., & McCreary, J. P., Jr (2009). Indian Ocean circulation and climate variability. *Reviews of Geophysics*, 47(1). <https://doi.org/10.1029/2007RG000245>
- Sengupta, D., Senan, R., Murty, V., & Fernando, V. (2004). A biweekly mode in the equatorial Indian Ocean. *Journal of Geophysical Research*, 109(C10). <https://doi.org/10.1029/2004JC002329>
- Smith, R., Jones, P., Briegleb, B., Bryan, F., Danabasoglu, G., Dennis, J., et al. (2010). The Parallel Ocean Program (POP) reference manual: Ocean component of the Community Climate System Model (CCSM) and Community Earth System Model (CESM). *LAUR-01853*, 141, 1–140.
- Smyth, W., Durland, T., & Moum, J. (2015). Energy and heat fluxes due to vertically propagating Yanai waves observed in the equatorial Indian Ocean. *Journal of Geophysical Research: Oceans*, 120(1), 1–15. <https://doi.org/10.1002/2014JC010152>

- Toole, J. M., Schmitt, R. W., Polzin, K. L., & Kunze, E. (1997). Near-boundary mixing above the flanks of a midlatitude seamount. *Journal of Geophysical Research*, *102*(C1), 947–959. <https://doi.org/10.1029/96JC03160>
- Wang, H., McClean, J. L., Talley, L. D., & Yeager, S. (2018). Seasonal cycle and annual reversal of the Somali Current in an eddy-resolving global ocean model. *Journal of Geophysical Research: Oceans*, *123*(9), 6562–6580. <https://doi.org/10.1029/2018JC013975>
- Wessel, P., Sandwell, D. T., & Kim, S.-S. (2010). The global seamount census. *Oceanography*, *23*(1), 24–33. <https://doi.org/10.5670/oceanog.2010.60>
- White, M., Bashmachnikov, I., Aristegui, J., & Martins, A. (2007). Physical processes and seamount productivity. *Seamounts: Ecology, Fisheries and Conservation*, 65–84.
- Wilkin, J. L., & Chapman, D. C. (1990). Scattering of coastal-trapped waves by irregularities in coastline and topography. *Journal of Physical Oceanography*, *20*(3), 396–421. [https://doi.org/10.1175/1520-0485\(1990\)020<0396:SOCTWB>2.0.CO;2](https://doi.org/10.1175/1520-0485(1990)020<0396:SOCTWB>2.0.CO;2)
- Yanai, M., & Murakami, M. (1970). Spectrum analysis of symmetric and antisymmetric equatorial waves. *Journal of the Meteorological Society of Japan Series II*, *48*(4), 331–347. https://doi.org/10.2151/jmsj1965.48.4_331
- Yokoi, T., Tozuka, T., & Yamagata, T. (2008). Seasonal variation of the Seychelles Dome. *Journal of Climate*, *21*(15), 3740–3754. <https://doi.org/10.1175/2008JCLI1957.1>